

Thesis
1158560

Observation and Inversion of Seismo-Acoustic Waves in a Complex Arctic Ice Environment

by

Bruce Edward Miller

B.S., United States Naval Academy (1975)

Submitted in partial fulfillment of the
requirements for the dual degrees of

OCEAN ENGINEER

and

MASTER OF SCIENCE IN OCEAN ENGINEERING

at the

MASSACHUSETTS INSTITUTE OF TECHNOLOGY

and the

WOODS HOLE OCEANOGRAPHIC INSTITUTION

September 1990

© Bruce Edward Miller, 1990

The author hereby grants to M.I.T., W.H.O.I. and the U.S. Government
permission to reproduce and to distribute copies of this thesis document in whole

Observation and Inversion of Seismo-Acoustic Waves in a Complex Arctic Ice Environment

by

Bruce Edward Miller

Submitted to the Massachusetts Institute of Technology/
Woods Hole Oceanographic Institution
Joint Program in Oceanographic Engineering
on August 10, 1990, in partial fulfillment of the
requirements for the degrees of
Ocean Engineer
and
Master of Science in Ocean Engineering

Abstract

The propagation of low frequency seismo-acoustic waves in the Arctic Ocean ice canopy is examined through the analysis of hydrophone and geophone data sets collected in 1987 at an ice camp designated PRUDEX in the Beaufort Sea.

Study of the geophone time series generated by under-ice explosive detonations reveals not only the expected longitudinal and flexural waves in the ice plate, but also an unexpected horizontally-polarized transverse (SH) wave arriving at a higher amplitude than the other wave types. The travel paths of all three observed wave types are found to be refracted in the horizontal plane along a line coincident with a known ridge separating the ice canopy locally into two distinct half-plates, the first of thin first year ice and the second of thicker multi-year ice. The origin of the SH wave appears to be near the detonation and not associated with the interaction of longitudinal, flexural or waterborne waves with the ridge line. The need to determine the exact location of each detonation from the received time series highlights the dramatic superiority of geophones over hydrophones in this application, as does the ability to detect the anomalous SH waves and the refracted ray paths, neither of which are visible in the hydrophone data.

Inversion of the geophone data sets for the low frequency elastic parameters of the ice is conducted initially by treating the ice as a single homogeneous isotropic plate to demonstrate the power of SAFARI numerical modeling in this application. A modified stationary phase approach is then used to extend SAFARI modeling to invert the data sets for the elastic parameters of the two ice half-plates simultaneously. The compressional/shear bulk wave speeds estimated in the half-plates, 3500/1750 m/s in the multi-year ice and 3000/1590 m/s in the new ice, are comparable to previously obtained values; however, the compressional/shear attenuation values in the two half-plates, 1.0/2.99 dB/ λ and 1.0/2.67 dB/ λ , respectively, are somewhat greater than previously measured values and four times greater than estimates extrapolated from high frequency data.

Thesis Supervisor: Dr. Henrik Schmidt
Massachusetts Institute of Technology

Acknowledgements

First and foremost, I am very deeply indebted to my thesis advisor, Professor Henrik Schmidt, for getting me started in the right direction and then providing an ideal research environment in which I have had the freedom to proceed as I saw fit, knowing that his sage counsel was immediately available to pull me through the rough spots. I can imagine no better student/advisor relationship than the one I have shared with him.

The faculty at MIT and WHOI have contributed greatly to my ability to complete this thesis by making so many complex subjects readily accessible to me. While each of my professors has contributed, I would like especially to acknowledge my debt to Professors Jim Lynch, Ira Dyer, Art Baggeroer and Al Oppenheim.

I certainly could not have completed much of this thesis without the support of three WHOI engineers: Eddie Scheer, Keith von der Heydt and Ken Prada. Their readiness to help has saved me from countless hours of worry and frustration. Similarly, the support of the administrative staff at WHOI and MIT, including Marilyn Staruch among many others, has been superb. Many of my fellow students, most notable among them Matt Sharpe, Randy Richards, Bob Headrick and Rob Fricke, have provided important assistance and advice.

I wish to express my most sincere thanks to the U.S. Navy and the Oceanographer of the Navy for providing the support for my studies in the Joint Program. I am particularly grateful to the Submarine Force for allowing me the opportunity to return to the academic world at this relatively late stage in my career.

Finally, there are no words sufficient to express my gratitude to my wife and son. Their cheerful support and seemingly inexhaustible patience during my many long hours at work have made this thesis possible.

Table of Contents

List of Figures	-6-
List of Tables	-9-
Chapter 1 Introduction	-10-
1.1 Motivation	-10-
1.2 Thesis Objectives	-11-
1.3 Thesis Content	-12-
Chapter 2 Theory	-15-
2.1 Propagation of Elastic Waves in a Plate	-15-
2.1.1 Elastic Waves in a Free Plate	-15-
2.1.2 Elastic Waves in a Floating Plate	-29-
2.2 Numerical Solutions	-31-
2.2.1 Full Wavefield Global Matrix Solution	-31-
2.2.2 Attenuation	-35-
Chapter 3 Experimental Measurements	-37-
3.1 The Experiments	-37-
3.2 The Observations	-41-
3.2.1 Hydrophone Data	-42-
3.2.2 Geophone Data	-43-
Chapter 4 Source Location	-49-
4.1 Localization Data	-49-
4.2 Localization Routine	-51-
4.3 Localization with Hydrophone Data	-53-
4.4 Shot Location using Geophone Data	-54-
4.4.1 Variations in Ice Thickness at the Receiving Array	-55-
4.4.2 Evidence for Refracted Waves	-56-
4.5 Locating the Source of the SH Wave	-63-
Chapter 5 Inversion of Propagation Data	-68-
5.1 Inversion Parameters	-68-
5.2 Previous Measurements	-69-
5.3 The Inversion Procedure	-70-
5.3.1 Inversion for an Infinite, Homogeneous Plate	-71-
5.3.2 Inversion of Two Abutting Infinite Half-Plates	-78-

Chapter 6 Conclusion -90-

 6.1 Summary -90-

 6.1.1 Elastic Parameters of the Arctic Ice -90-

 6.1.2 Propagation Mechanisms -91-

 6.1.3 Analysis Tools -91-

 6.2 Future Work -93-

References -95-

List of Figures

Figure 2-1: Two dimensional geometry for infinite plate of thickness $2h$ bounded by vacuum above and vacuum or liquid below.	-16-
Figure 2-2: Frequency spectrum, $\bar{k}_x=(2h/\pi)k_x$ versus $\bar{k}_y=(2h/\pi)k_y$, for $\nu=0.31$, showing symmetric (thick lines) and anti-symmetric(dotted lines) modes (from Mindlin [9]).	-24-
Figure 2-3: A symmetric (longitudinal) wave u_x in a free plate seen as the superposition of a pair of P waves and a pair of SV waves incident on the faces of the plate (after Redwood [11]).	-26-
Figure 2-4: Frequency spectrum, \bar{k}_x versus \bar{k}_y , for the symmetric(-) and antisymmetric(--) SH modes of an infinite free plate (after Graff [7]).	-28-
Figure 3-1: PRUDEX hydrophone and geophone array layout on the x/y plane used throughout this paper, hydrophones H0-H15 suspended at a 60 meter water depth, geophones G1-G4 frozen into the ice.	-38-
Figure 3-2: Waterborne acoustic waves as recorded at the output of PRUDEX array hydrophones (from top to bottom) #8, #3 and #0 in response to experimental under-ice shot number F3.	-42-
Figure 3-3: PRUDEX geophone array layout showing alignment of principal axes on each geophone.	-43-
Figure 3-4: Time series as observed in the (top to bottom) radial, transverse and vertical directions on PRUDEX geophone #4 in response to experimental shot F3.	-45-
Figure 3-5: Vertical geophone #4 response for experimental shots F3(-) and F4(-); <u>top</u> , the response to the waterborne acoustic wave as it passes under the ice, and <u>bottom</u> , the flexural wave.	-47-
Figure 3-6: Hodograph for the x and y axes of geophone #3 showing the response to shot F4 at times from 0.1 to 0.323 seconds(-) and 0.323 to 0.5 seconds(-) after detonation.	-48-
Figure 4-1: Temperature/Salinity/Sound Speed profiles at the PRUDEX ice camp, 31 March 1987, 0601 U.T. (from McPhee [16]).	-51-
Figure 4-2: $\Delta\chi^2$ Contours for the best fit location for the F series of shots calculated using hydrophone array data, plotted with the best fit locations(+) for Monte Carlo simulations of that data.	-55-
Figure 4-3: Plot of PRUDEX array layout showing apparent axis of arrival of (1) both the hydrophone and geophone water waves, (2) the SH wave, (3) the longitudinal wave, and (4) the flexural wave.	-58-
Figure 4-4: $\Delta\chi^2$ contours (in dB) for the best fit ridge line orientation, described by the line $y=mx+b$ on an x/y plane centered on the horizontal plane of the array with geophone #4 on the x-axis.	-60-

Figure 4-5: Plan showing on an x-y plane the PRUDEX geophone(*) and hydrophone(+) array, the best location for the F series of shots(x), the best fit ridge line(--), and the longitudinal wave paths from shot to each geophone(...).	-60-
Figure 4-6: Aerial photograph of the PRUDEX ice camp and array, showing locations of identifiable hydrophones (geophones and some hydrophones are not visible), the array axis and the ice ridge line.	-61-
Figure 4-7: $\Delta\chi^2$ contours (in dB) for the best fit location for the F series of shots calculated using geophone data, plotted with the best fit locations for 80 Monte Carlo simulations(+) of that data.	-62-
Figure 4-8: Plots of the 90% confidence limit ellipses for the F series shot location derived from geophone and hydrophone data.	-64-
Figure 4-9: $\Delta\chi^2$ contours (in dB) generated by the shot location routine for the SH wave point of origin(-) assuming the time of origin is fixed at shot time, with contours for the best fit shot location(-) of section 4.4. . . .	-65-
Figure 4-10: $\Delta\chi^2$ contours (in dB) generated by the shot location routine for the point of origin of the SH wave with time of origin fixed at the average time of longitudinal waves' (...) arrival at the ridge line (--).	-66-
Figure 4-11: $\Delta\chi^2$ contours (in dB) generated by the location routine for the point of origin of the SH wave with the time origin fixed at the time of the waterborne waves' (...) arrival at the ridge line(--).	-67-
Figure 5-1: Two sets of dispersion curves for flexural waves in ice at shear velocities $\beta=1600\text{m/s}$ (--) and $\beta=1800\text{m/s}$ (...), and (top to bottom in each set) ice thicknesses of 1.25, 1.15 and 1.05m.	-74-
Figure 5-2: Two sets of group velocity curves for longitudinal waves in ice with compressional velocities of 3500m/s(...) and 3400m/s(--) and shear velocities (top to bottom in each set) of 1800, 1700 and 1600 m/s. . . .	-75-
Figure 5-3: Synthetic time series for the pressure signature at 1 meter for an explosive charge simulating shot F3; <u>top</u> , sampled at 10 KHz, and <u>bottom</u> , prefiltered and decimated to 1000 Hz.	-76-
Figure 5-4: <u>Top</u> , synthetic time series of Figure 5-3 filtered to a 2-90 Hz band, and <u>bottom</u> , spectrum of filtered time series.	-76-
Figure 5-5: Spectrum of signal received on vertical component of geophone #3 during experimental shot F3, showing preponderance of energy in the 2-90 Hz band.	-77-
Figure 5-6: Observed contours of spectrum level (in dB normalized to 0 dB maximum) obtained by combining data from 8 shots at the PRUDEX ice camp, with the dispersion curve (-) calculated for $\beta=1700\text{m/s}$ and $2h=1.31$	-79-
Figure 5-7: Synthetic contours of spectrum level (in dB, normalized to 0 dB maximum) derived from SAFARI time series calculated for $\alpha=3400\text{ m/s}$, $\beta=1700\text{ m/s}$, $2h=1.31\text{m}$, with corresponding exact dispersion curve(--).	-79-

Figure 5-8: Observed response(-) on radial geophone #3 for PRUDEX shot F3; SAFARI synthetic radial response(-·) for $\alpha=3400\text{m/s}$, $\beta=1700\text{m/s}$, $2h=1.31\text{m}$, $\gamma_\alpha=1.0\text{dB}/\lambda$, $\gamma_\beta=2.99\text{dB}/\lambda$	-80-
Figure 5-9: Observed response(-) on vertical geophone #3 for PRUDEX shot F3; SAFARI synthetic vertical response(-·) for $\alpha=3400\text{m/s}$, $\beta=1700\text{m/s}$, $2h=1.31\text{m}$, $\gamma_\alpha=1\text{dB}/\lambda$, $\gamma_\beta=2.99\text{dB}/\lambda$	-80-
Figure 5-10: Synthetic time series for the flexural wave in a floating ice plate, calculated by SAFARI for $\alpha=3500\text{m/s}$, $\beta=1750\text{m/s}$, $2h=2.4\text{m}$, $\gamma_\alpha=1.0\text{dB}/\lambda$, $\gamma_\beta=2.99\text{dB}/\lambda$ at a range of 242m.	-84-
Figure 5-11: SAFARI synthetic time series(-) for parameters of Figure 5-10 at a range of 569.5m, and time series(-·) generated by applying the method of stationary phase to Figure 5-10.	-84-
Figure 5-12: Observed flexural wave time series(-) for PRUDEX shot F3 at vertical geophone #4, and synthetic time series(-·) for shot F3 at geophone #4 developed using the parameters of Table 5-2.	-87-
Figure 5-13: Observed flexural wave time series(-) for PRUDEX shot F3 at vertical geophone #3, and synthetic time series(-·) for shot F3 at geophone #3 developed using the parameters of Table 5-2.	-87-
Figure 5-14: Observed flexural wave time series(-) for PRUDEX shot F3 at vertical geophone #1, and synthetic time series(-·) for shot F3 at geophone #1 developed using the parameters of Table 5-2.	-88-
Figure 5-15: Observed flexural wave time series(-) for PRUDEX shot F3 at vertical geophone #2, and synthetic time series(-·) for shot F3 at geophone #2 developed using the parameters of Table 5-2.	-88-

List of Tables

Table 3-1: Summary of experimental shots recorded during PRUDEX propagation experiments. (*) indicates no depth recorded on shot log, "cord" refers to primacord, "drams" to explosive weight.	-40-
Table 4-1: Deviations from the average ice thickness determined at each geophone in the PRUDEX array.	-57-
Table 5-1: Summary of recent measurements of the elastic parameters of arctic sea ice at low frequency.	-71-
Table 5-2: Best compressional/shear velocities and attenuations and plate thicknesses determined by treating the PRUDEX ice cover as two abutting half-plates, with the shot conducted under plate 1, and the receiving array on plate 2.	-86-

Chapter 1

Introduction

The introduction describes the motivation and objectives for this thesis, and reviews its organization and content by chapter.

1.1 Motivation

The Arctic Ocean has grown increasingly important to national strategic interests in recent years; yet our understanding of the Arctic Ocean environment has lagged far behind that of the other major ocean systems. In particular, the modeling of low frequency acoustic propagation under the sea ice canopy in the Arctic Ocean has proven to be an elusive problem [1]. The difficulty has not been in general that the necessary tools to do this modeling are unavailable. For instance, Schmidt's Fast Field algorithm, SAFARI [2], has proven to be a very capable package for solving propagation problems in a complex seismo-acoustic environment such as is presented by the deep Arctic. The difficulty has been that very little work has been done to obtain measurements of the starting parameters crucial to computing this propagation accurately, *i.e.*, the elastic parameters of the ice canopy - compressional and shear wave bulk velocities and attenuation factors. As a result, previous modeling has been based largely on parameters measured in the laboratory or extrapolated from somewhat similar environments (freshwater lake ice, glacial ice, *etc.*). Recent investigations have suggested that parameters so obtained do not accurately reflect the Arctic environment,

and that measurements of the elastic parameters of the arctic ice are needed *in situ* before we can hope to model acoustic propagation in the Arctic Ocean accurately.

1.2 Thesis Objectives

The overall objective of this work is to improve our ability to accurately model acoustic propagation in the Arctic Ocean. To this end, data sets obtained in 1987 during seismo-acoustic propagation experiments conducted at an ice camp in the Beaufort Sea designated PRUDEX are studied extensively. The initial intent of this study was simply to apply advanced modeling techniques to the problem of inverting the hydrophone and geophone data as received at the PRUDEX arrays to obtain accurate measurements of the elastic parameters. Although inversion to obtain elastic parameters remains the focus of this work, unexpected phenomena observed in the propagation data have served to partially frustrate the immediate goal of obtaining the elastic parameters by increasing the difficulty of the inversion, while simultaneously contributing to the overall understanding of seismo-acoustic propagation in the Arctic by disclosing mechanisms in the propagation previously unobserved or unsuspected. In particular, arrivals characteristic of the refraction of all types of propagating waves at a linear discontinuity in the horizontal plane of the ice plate are presented. The author also attempts with apparent success to model this refraction and extend the inversion to obtain the elastic parameters of two separate kinds of ice cover, annual ice and multi-year ice, simultaneously. More importantly, completely unexpected horizontally polarized transverse (SH mode) waves are presented in the propagation data. Although the existing theories of seismo-acoustic propagation in an elastic plate have no mechanism by which an underwater explosion can generate SH waves in a sheet of ice floating over that explosion, these waves are present in the PRUDEX data sets at amplitudes greater

than any other wave type observed. These waves are important because their creation by out-of-plane scattering of other wave types may be a significant and heretofore unknown mechanism for the attenuation of acoustic energy entering the ice cover from the water. In addition to identifying their existence in the PRUDEX data, as a first step toward understanding their origin, the author investigates possible source locations for the SH waves relative the explosive source, the other wave types in the ice, and known discontinuities in the ice cover.

1.3 Thesis Content

Chapter 2 of this thesis lays the foundation for later work by reviewing the theory of wave propagation in a thin elastic plate under various conditions, focusing on the development of the three wave types commonly observed in such plates, the longitudinal plate wave, the flexural wave, and the transversely polarized SH wave. The second chapter then reviews briefly the numerical modeling tool used throughout this work, Schmidt's SAFARI algorithm [3]. Chapter 2 concludes with a short discussion of the approach to the attenuation of elastic waves employed in this work.

The third chapter introduces the reader to the experimental data as obtained at the PRUDEX ice camp. The background for the experiments is reviewed to make clear the need to determine through the analysis of seismo-acoustic propagation data some parameters which could have been measured precisely during the experiment. The nature of the acoustic source pulse used during the experiments, a key factor in later analysis, is described and explained using data received at a hydrophone array. Finally, the occurrence of the three principal wave types is identified in the data received at the experiment's geophone array.

Chapter 4 exists principally because the location and time of the underwater

explosive detonations used to excite seismo-acoustic propagation in the ice cover were not recorded relative to the receiving arrays during the PRUDEX experiments. In the process of determining shot time and location for use in later inversion, this chapter brings out the somewhat startling result that a simple array of four 3-axis geophones can be a much more effective tool for locating underwater sources than a larger hydrophone array in the water below the geophones. Geophone data is used in Chapter 4 not only to determine a much more accurate source location than is available using hydrophone data, but also to identify and analyze the refraction at the joint between two abutting ice half-plates of all wave types propagating in the horizontal plane of the ice sheet. Chapter 4 also reviews the evidence available to help identify the origin of the high amplitude SH waves which are visible only in the geophone data.

Chapter 5 begins by explaining the fundamentals of the process of inverting response data for the elastic parameters of the propagating media, and then reviews previous work done to determine those parameters in arctic sea ice. The description and results of the inversion obtained by treating the ice canopy as a single homogeneous isotropic plate follow. These results serve to demonstrate the potential of SAFARI modeling of wave propagation; although based on the work of Chapter 4, the ice is more accurately modeled as two abutting half-plates with significantly different elastic parameters, and the results obtained by the single plate model are of questionable accuracy. To solve this problem, Chapter 5 introduces a method for using stationary phase analysis [4] in a somewhat modified form to extend two-dimensional SAFARI to model propagation of the flexural wave in the range dependent environment of the two abutting half-plates. The results of inversion using this modeling technique are then presented.

Chapter 6 summarizes the results of Chapters 3, 4 and 5 and establishes their

importance relative to seismo-acoustic propagation in the Arctic Ocean. Chapter 6 also comments on additional work needed in this area.

Chapter 2

Theory

Prior to beginning the evaluation and analysis of any experimental data, it is important to have a firm underpinning in the theory behind that data. This chapter will review briefly the fundamental theory of propagation of elastic waves in an ice plate and the equations which characterize that propagation. It will then describe the principal tool used in this paper to solve these equations numerically, Schmidt's SAFARI algorithms [3].

2.1 Propagation of Elastic Waves in a Plate

An understanding of the unique characteristics of wave propagation in a thin elastic plate is essential to the study of seismo-acoustic waves in the arctic ice. Three fundamental wave types, longitudinal waves, flexural waves and horizontally-polarized transverse (SH) waves are commonly observed propagating in floating ice sheets [5][6]. It is useful to look first at the origins of the three wave types in a free elastic plate and then extend those results to a plate bounded by a liquid half-space on one side and a vacuum (or air) on the other.

2.1.1 Elastic Waves in a Free Plate

Consider waves propagating in the positive x direction in a laterally infinite homogeneous isotropic plate bounded on both sides by vacuum as shown in Figure 2-1.

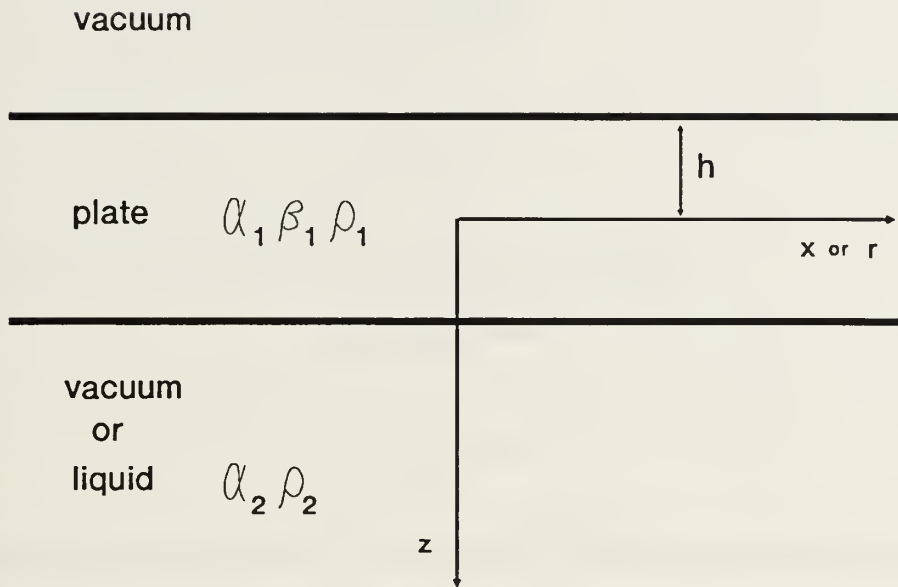


Figure 2-1: Two dimensional geometry for infinite plate of thickness $2h$ bounded by vacuum above and vacuum or liquid below.

If displacements in the plate satisfy the Navier equation,

$$\rho \bar{\mathbf{u}} = \bar{\mathbf{f}} + (\lambda + 2\mu) \nabla(\nabla \cdot \bar{\mathbf{u}}) - \mu \nabla \times (\nabla \times \bar{\mathbf{u}}) \quad , \quad (2.1)$$

where λ and μ are the Lamé constants, then Lamé's theorem states [4] that a scalar potential ϕ and a vector potential $\bar{\Psi}$ exist which satisfy

$$\bar{\mathbf{u}} = \nabla \phi + \nabla \times \bar{\Psi} \quad (2.2)$$

$$\nabla \cdot \bar{\Psi} = 0 \quad (2.3)$$

$$\nabla^2 \phi = \frac{1}{\alpha^2} \ddot{\phi} \quad (2.4)$$

$$\nabla^2 \bar{\Psi} = \frac{1}{\beta^2} \ddot{\bar{\Psi}} \quad , \quad (2.5)$$

where

$$\alpha^2 = \frac{\lambda + 2\mu}{\rho} \quad (2.6)$$

$$\beta^2 = \frac{\mu}{\rho} . \quad (2.7)$$

As a trial solution, consider plane wave solutions of the form

$$\phi = f(z)e^{i(k_x x - \omega t)} \quad (2.8)$$

$$\bar{\psi} = \bar{h}(z)e^{i(k_x x - \omega t)} . \quad (2.9)$$

Substitution of these solutions into (2.2) through (2.5) yields the following set of four equations in eight unknowns for the potentials,

$$\phi = A^- e^{i(k_x x - k_{z\alpha} z - \omega t)} + A^+ e^{i(k_x x + k_{z\alpha} z - \omega t)} \quad (2.10)$$

$$\psi_x = B^- e^{i(k_x x - k_{z\beta} z - \omega t)} + B^+ e^{i(k_x x + k_{z\beta} z - \omega t)} \quad (2.11)$$

$$\psi_y = C^- e^{i(k_x x - k_{z\beta} z - \omega t)} + C^+ e^{i(k_x x + k_{z\beta} z - \omega t)} \quad (2.12)$$

$$\psi_z = D^- e^{i(k_x x - k_{z\beta} z - \omega t)} + D^+ e^{i(k_x x + k_{z\beta} z - \omega t)} . \quad (2.13)$$

The wave nature of the potentials, and thus the motion, is clearly seen in these equations.

(2.10) through (2.13) can be used to develop seismo-acoustic propagation in any layered (two dimensional) environment, and various types of body and surface waves arise depending upon the media and the boundary conditions. The quantities α and β are the compressional (P-wave) and shear (SV/SH-waves) bulk velocities; k_x is the

horizontal wavenumber and $k_{z\alpha}$ and $k_{z\beta}$ are the vertical wavenumbers for compressional and shear waves. No attempt is made in this paper to review the theory supporting any propagation other than that occurring in a thin elastic plate; although references to other wave types are used to relate propagation in the thin elastic plate to other results for readers familiar with seismo-acoustics.

From this point, one of the most complete developments of the basic characteristics of waves in a free plate is provided by Graff based on work by Meeker and Meitzler [7]. For simplicity in following this development, (2.10) through (2.13) are rewritten in terms of sines and cosines (with different constants),

$$\phi = (A\cos k_{z\alpha}z + B\sin k_{z\alpha}z)e^{i(k_x x - \omega t)} \quad (2.14)$$

$$\psi_x = (C\cos k_{z\beta}z + D\sin k_{z\beta}z)e^{i(k_x x - \omega t)} \quad (2.15)$$

$$\psi_y = (E\cos k_{z\beta}z + F\sin k_{z\beta}z)e^{i(k_x x - \omega t)} \quad (2.16)$$

$$\psi_z = (G\cos k_{z\beta}z + H\sin k_{z\beta}z)e^{i(k_x x - \omega t)} . \quad (2.17)$$

If (2.2) is simplified for dependence only on x and z in the two dimensional problem under consideration, and the potentials of (2.14) through (2.17) are substituted into the result, then particle displacements are given by

$$\begin{aligned} u_x &= \frac{\partial \phi}{\partial x} + \frac{\partial \psi_y}{\partial z} \\ &= [ik_x(A\cos k_{z\alpha}z + B\sin k_{z\alpha}z) + k_{z\beta}(-E\sin k_{z\beta}z + F\cos k_{z\beta}z)]e^{i(k_x x - \omega t)} \end{aligned} \quad (2.18)$$

$$\begin{aligned}
u_y &= -\frac{\partial \psi_x}{\partial z} + \frac{\partial \psi_z}{\partial x} \\
&= [-k_{z\beta}(-C\sin K_{z\beta}z + D\cos k_{z\beta}z) + ik_x(G\cos k_{z\beta}z + H\sin k_{z\beta}z)]e^{i(k_x x - \omega t)}
\end{aligned} \tag{2.19}$$

$$\begin{aligned}
u_z &= \frac{\partial \phi}{\partial z} - \frac{\partial \psi_y}{\partial x} \\
&= [k_{z\alpha}(-A\sin K_{z\alpha}z + B\cos k_{z\alpha}z) - ik_x(E\cos k_{z\beta}z + F\sin k_{z\beta}z)]e^{i(k_x x - \omega t)}.
\end{aligned} \tag{2.20}$$

The basic nature of wave motion in elastic solids emerges from (2.18) through (2.20) in the decoupling of transverse (SH) motion from radial and vertical motion (SV/P); u_y depends on ψ_x and ψ_z , while u_x and u_z depend on ψ_y and ϕ .

The generalized form of Hooke's law for the stress tensor, τ_{ij} , in a linearly elastic solid,

$$\tau_{ij} = C_{ijpq} e_{pq}, \tag{2.21}$$

where the strain tensor, e_{ij} , is given by

$$e_{ij} = \frac{1}{2}(u_{i,j} + u_{j,i}), \tag{2.22}$$

reduces in the homogeneous isotropic plate to

$$\begin{aligned}
\tau_{zz} &= (\lambda + 2\mu) \frac{\partial u_z}{\partial z} + \lambda \frac{\partial u_x}{\partial x}, \\
\tau_{zx} &= \mu \left(\frac{\partial u_z}{\partial x} + \frac{\partial u_x}{\partial z} \right), \\
\tau_{zy} &= \mu \frac{\partial u_y}{\partial y}.
\end{aligned} \tag{2.23}$$

On the upper and lower faces of the plate ($z=\pm h$) the boundary conditions between plate and vacuum are simply

$$\tau_{zz} = \tau_{zx} = \tau_{yz} = 0, \quad z = \pm h . \quad (2.24)$$

Equations (2.18) through (2.20), (2.23) and (2.24) combine to form 6 equations in the eight unknowns A, B, C, D, E, F, G and H. Recalling that Lamé's theorem also provides that the divergence of the vector potential is zero (2.3), in the simplified geometry of the plate this relation becomes

$$\frac{\partial \psi_x}{\partial x} + \frac{\partial \psi_z}{\partial z} = 0 . \quad (2.25)$$

Substituting (2.15) and (2.17) into (2.25) yields two additional equations, for a total of eight equations in the eight unknowns. In matrix form this system of 8 equations is written as

$$\begin{bmatrix} ac_\alpha & as_\alpha & 0 & 0 & -bs_\beta & bc_\beta & 0 & 0 \\ ac_\alpha & -as_\alpha & 0 & 0 & bs_\beta & bc_\beta & 0 & 0 \\ 0 & 0 & cc_\beta & cs_\beta & 0 & 0 & -ds_\beta & dc_\beta \\ 0 & 0 & cc_\beta & -cs_\beta & 0 & 0 & ds_\beta & dc_\beta \\ -es_\alpha & ec_\alpha & 0 & 0 & fc_\beta & fs_\beta & 0 & 0 \\ es_\alpha & ec_\alpha & 0 & 0 & fc_\beta & -fs_\beta & 0 & 0 \\ 0 & 0 & gc_\beta & gs_\beta & 0 & 0 & -hs_\beta & hc_\beta \\ 0 & 0 & gc_\beta & -gs_\beta & 0 & 0 & hs_\beta & hc_\beta \end{bmatrix} \cdot \begin{bmatrix} A \\ B \\ C \\ D \\ E \\ F \\ G \\ H \end{bmatrix} = 0 , \quad (2.26)$$

where

$$\begin{aligned}
a &= (\lambda + 2\mu)k_{z\alpha}^2 + \lambda k_x^2 & h &= k_{z\beta} \\
b &= 2i\mu k_x k_{z\beta} & g &= ik_x \\
c &= k_{z\beta}^2 & c_\alpha &= \cos k_{z\alpha} h \\
d &= ik_x k_{z\beta} & s_\alpha &= \sin k_{z\alpha} h \\
e &= 2ik_x k_{z\alpha} & c_\beta &= \cos k_{z\beta} h \\
f &= k_x^2 - k_{z\beta}^2 & s_\beta &= \sin k_{z\beta} h .
\end{aligned} \tag{2.27}$$

Using a number of straightforward matrix manipulations, it is easy to show that the system of (2.26) is equivalent to

$$\begin{bmatrix}
as_\alpha & -bs_\beta & 0 & 0 & 0 & 0 & 0 & 0 \\
ec_\alpha & fc_\beta & 0 & 0 & 0 & 0 & 0 & 0 \\
0 & 0 & -ds_\beta & cs_\beta & 0 & 0 & 0 & 0 \\
0 & 0 & -hs_\beta & gs_\beta & 0 & 0 & 0 & 0 \\
0 & 0 & 0 & 0 & -es_\alpha & fs_\beta & 0 & 0 \\
0 & 0 & 0 & 0 & ac_\alpha & bc_\beta & 0 & 0 \\
0 & 0 & 0 & 0 & 0 & 0 & cc_\beta & dc_\beta \\
0 & 0 & 0 & 0 & 0 & 0 & gc_\beta & hc_\beta
\end{bmatrix} \cdot \begin{bmatrix} B \\ E \\ G \\ D \\ A \\ F \\ C \\ H \end{bmatrix} = 0 . \tag{2.28}$$

A necessary and sufficient condition for the existence of a solution to the homogeneous system $Ax=0$ is that $\det(A)=0$ [8]. The format of (2.28) is advantageous because the determinant of that special form of an 8x8 matrix expands to the simple form

$$\begin{vmatrix} as_\alpha & -bs_\beta \\ ec_\alpha & fc_\beta \end{vmatrix} \cdot \begin{vmatrix} -ds_\beta & cs_\beta \\ -hs_\beta & gs_\beta \end{vmatrix} \cdot \begin{vmatrix} -es_\alpha & fs_\beta \\ ac_\alpha & bc_\beta \end{vmatrix} \cdot \begin{vmatrix} cc_\beta & dc_\beta \\ gc_\beta & hc_\beta \end{vmatrix} = 0 , \tag{2.29}$$

where coefficients B and E are associated only with the elements of the first, G and D the second, A and F the third, and C and H the fourth determinant in (2.29). Thus four separate solutions to (2.28) must exist, such that only the pair of coefficients associated

with each 2x2 determinant is non-zero, while the other six coefficients vanish.

Looking first at the coefficient pairs A/F and B/E, if only A,F≠0, then substitution in (2.18) through (2.20) yields

$$\begin{aligned} u_x &= (ik_x A \cos k_{z\alpha} z + k_{z\beta} F \cos k_{z\beta} z) e^{i(k_x x - \omega t)} \\ u_y &= 0 \\ u_z &= (-k_{z\alpha} A \sin k_{z\alpha} z - ik_x F \sin k_{z\beta} z) e^{i(k_x x - \omega t)} , \end{aligned} \quad (2.30)$$

and if only B,E≠0, the same substitution produces

$$\begin{aligned} u_x &= (ik_x B \sin k_{z\alpha} z - k_{z\beta} E \sin k_{z\beta} z) e^{i(k_x x - \omega t)} \\ u_y &= 0 \\ u_z &= (k_{z\alpha} B \cos k_{z\alpha} z - ik_x E \cos k_{z\beta} z) e^{i(k_x x - \omega t)} . \end{aligned} \quad (2.31)$$

Solutions (2.30) and (2.31) are polarized in the longitudinal and vertical directions only; (2.30) is symmetric with respect to the x/y plane while (2.31) is antisymmetric with respect to the x/y plane. Additionally, setting the 2x2 determinant in (2.29) associated with each solution's coefficient pair to zero generates an equation which describes the required relation between vertical and horizontal wave numbers for that solution to exist, *i.e.*, the frequency equation for that solution. Setting the 2x2 determinant for coefficients A and F to zero yields

$$-es_\alpha bc_\beta - fs_\beta ac_\alpha = 0 , \quad (2.32)$$

which can be rewritten as

$$\frac{\tan k_{z\beta} h}{\tan k_{z\alpha} h} = -\frac{-4\mu k_x^2 k_{z\alpha} k_{z\beta}}{(k_x^2 - k_{z\beta}^2)((\lambda + 2\mu)k_{z\alpha}^2 + \lambda k_x^2)} , \quad (2.33)$$

and since

$$\begin{aligned}
\frac{\mu}{(\lambda+2\mu)k_{z\alpha}^2 + \lambda k_x^2} &= \frac{\mu}{(\lambda+2\mu)(k_{z\alpha}^2 + k_x^2) - 2\mu k_x^2} \\
&= \frac{1}{\left(\frac{\lambda+2\mu}{\mu}\right)k_{z\alpha}^2 - 2k_x^2} \\
&= \frac{1}{\frac{\alpha^2}{\beta^2}k_{z\alpha}^2 - 2k_x^2} = \frac{1}{k_{z\beta}^2 - 2k_x^2} \\
&= \frac{1}{k_{z\beta}^2 - k_x^2},
\end{aligned} \tag{2.34}$$

where

$$k_{\alpha}^2 = k_x^2 + k_{z\alpha}^2 \quad \text{and} \quad k_{\beta}^2 = k_x^2 + k_{z\beta}^2, \tag{2.35}$$

(2.33) becomes

$$\frac{\tan k_{z\beta} h}{\tan k_{z\alpha} h} = -\frac{4k_x^2 k_{z\alpha} k_{z\beta}}{(k_x - k_{z\beta})^2}. \tag{2.36}$$

(2.36) is the well known Rayleigh-Lamb frequency equation for symmetric plate waves.

In the antisymmetric case (coefficients B, E ≠ 0) the determinant yields similarly

$$\frac{\tan k_{z\beta} h}{\tan k_{z\alpha} h} = -\frac{(k_x - k_{z\beta})^2}{4k_x^2 k_{z\alpha} k_{z\beta}}. \tag{2.37}$$

Although (2.36) and (2.37) were originally obtained slightly more than 100 years ago by Rayleigh and Lamb, the associated frequency spectrum was not completely understood until much later. Figure 2-2 illustrates the complete free plate frequency spectrum as obtained by Mindlin [9] for a value of Poisson's ratio of $\nu=0.31$. In Figure 2-2 the (positive or negative) real and imaginary values of $\bar{k}_x = (2h/\pi)k_x$ are

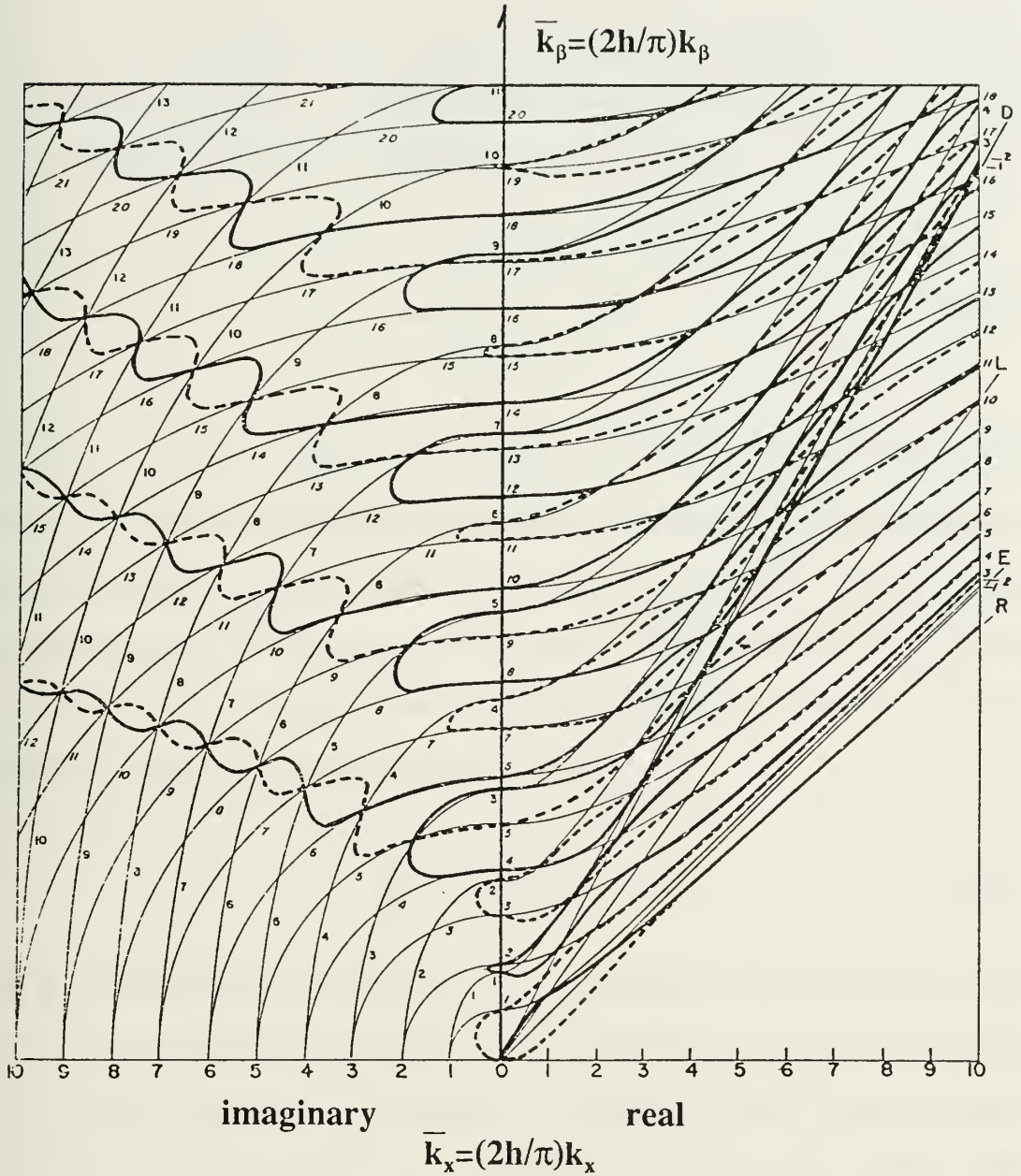


Figure 2-2: Frequency spectrum, $\bar{k}_x = (2h/\pi)k_x$ versus $\bar{k}_\beta = (2h/\pi)k_\beta$, for $\nu=0.31$, showing symmetric (thick lines) and anti-symmetric (dotted lines) modes (from Mindlin [9]).

plotted against $\bar{k}_\beta = (2h/\pi)k_\beta$. While the periodic nature of the tangent function introduces an infinity of modes, Figure 2-2 also shows that except for the lowest order fundamental symmetric and anti-symmetric modes, all modes have a cutoff frequency

below which the propagating wavenumbers are imaginary and waves are evanescent in the horizontal direction. The cutoff frequencies for the first symmetric and antisymmetric modes above the fundamental ones are given by

$$\begin{aligned} k_{\alpha}h &= \frac{\pi}{2} \\ \text{and} \\ k_{\beta}h &= \frac{\pi}{2} \end{aligned} \quad (2.38)$$

respectively [7]. Treating a typical arctic ice sheet ($h=3\text{m}$, $\alpha=3500\text{m/s}$, $\beta=1800\text{m/s}$ [14]) as a free plate, below about 300 Hz only the fundamental antisymmetric and symmetric modes can propagate. Further, for the case in which the wavelength is long compared to the thickness of the plate (thin plate assumption), i.e., $k_{\alpha}h \rightarrow 0$ and $k_{\beta}h \rightarrow 0$, (2.36) can be reduced easily to a simple expression for the fundamental symmetric mode by replacing the tangent functions with their arguments

$$\frac{c_p^2}{\beta^2} = 4 \left(1 - \frac{\beta^2}{\alpha^2} \right), \quad (2.39)$$

where c_p is the phase speed for the wave. The lowest order symmetric mode in a thin plate is called the longitudinal or plate wave. The longitudinal wave is non-dispersive in the thin plate limit since (2.39) indicates that the phase speed is not dependent on frequency. A similar expression can be obtained for the lowest order mode of the antisymmetric case in the thin plate limit. By replacing the tangent function with its Taylor series and discarding higher order terms, (2.37) reduces to

$$\frac{c_f^2}{\beta^2} = \frac{4}{3} k_x^2 h^2 \left(1 - \frac{\beta^2}{\alpha^2} \right). \quad (2.40)$$

Here c_f is the phase speed for the lowest order antisymmetric wave, generally referred

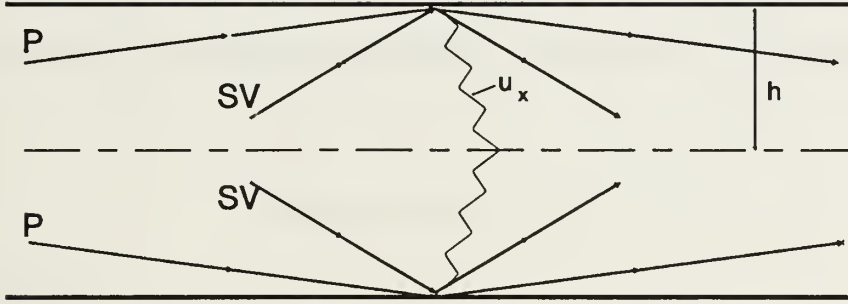


Figure 2-3: A symmetric (longitudinal) wave u_x in a free plate seen as the superposition of a pair of P waves and a pair of SV waves incident on the faces of the plate (after Redwood [11]).

to as the flexural wave. The flexural wave is clearly a dispersive wave. As implied by the form of (2.30) and (2.31), longitudinal and flexural waves in a free plate may be thought of as constructive interference of multiply-reflected P and SV body waves [10]. Figure 2-3 (after Redwood [11]) demonstrates this point of view for a longitudinal wave.

Looking now at the remaining two coefficient pairs in (2.28), if only $C, H \neq 0$, then substitution in (2.18) through (2.20) produces

$$\begin{aligned} u_x &= u_z = 0 \\ u_y &= [(k_{z\beta} C + i k_x H) \sin k_{z\beta} z] e^{i(k_x x - \omega t)}, \end{aligned} \quad (2.41)$$

and if only $D, G \neq 0$, then the same substitution produces

$$\begin{aligned} u_x &= u_z = 0 \\ u_y &= [(-k_{z\beta} D + i k_x G) \cos k_{z\beta} z] e^{i(k_x x - \omega t)} . \end{aligned} \quad (2.42)$$

These two solutions are transversely polarized SH waves; (2.41) is antisymmetric with respect to the x/z plane, and (2.42) symmetric with respect to the x/z plane. The frequency equation from the 2x2 determinant in (2.29) associated with the antisymmetric case is

$$c c_\beta h c_\beta - d c_\beta g c_\beta = 0 , \quad (2.43)$$

which simplifies to

$$k_{z\beta} (k_{z\beta}^2 + k_x^2) \cos^2 k_{z\beta} h = 0 . \quad (2.44)$$

Solutions to (2.44) exist only for

$$k_{z\beta} h = \frac{(2n+1)\pi}{2} , \quad n=0,1,2,3,\dots . \quad (2.45)$$

Similarly, for the symmetric case

$$k_{z\beta} (k_{z\beta}^2 + k_x^2) \sin^2 k_{z\beta} h = 0 , \quad (2.46)$$

for which solutions exist only for

$$k_{z\beta} h = m\pi , \quad m=0,1,2,3,\dots . \quad (2.47)$$

If the results of (2.45) and (2.47) are combined, then SH mode solutions exist for

$$k_{z\beta} h = \frac{n\pi}{2} , \quad n=0,1,2,3,\dots , \quad (2.48)$$

with n odd the antisymmetric and n even the antisymmetric modes. (2.48) can be shifted to a more revealing form by writing it in terms of k_β and k_x ,

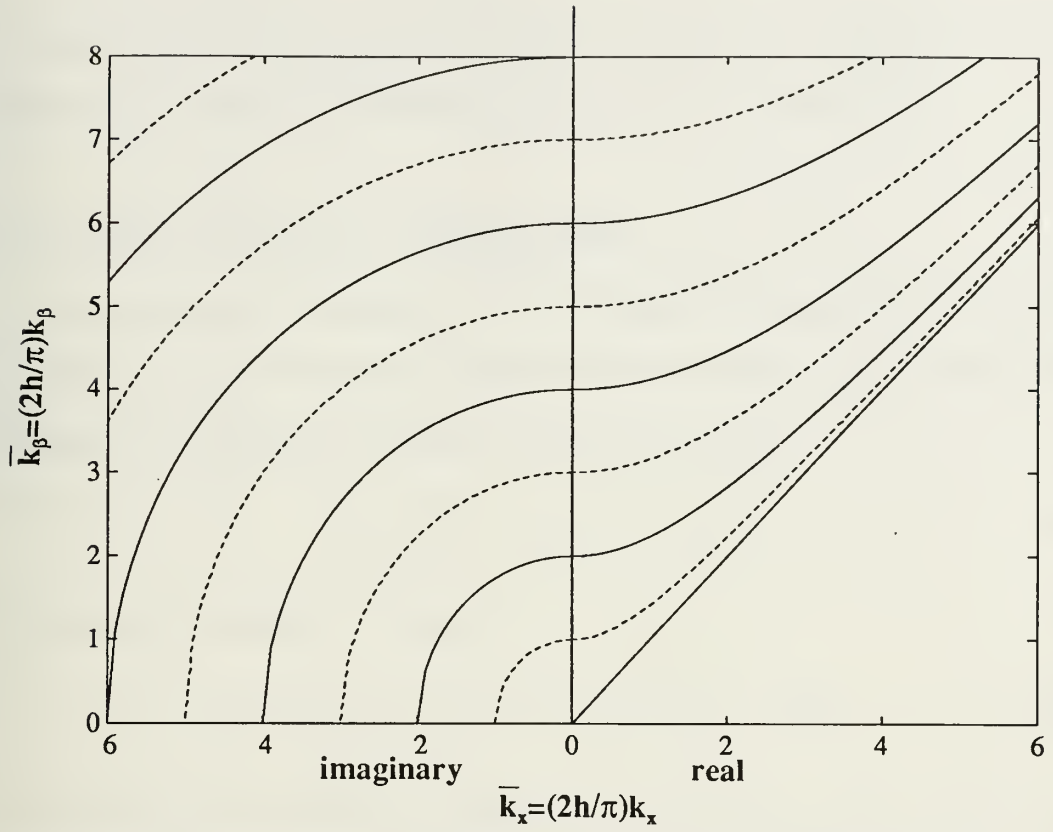


Figure 2-4: Frequency spectrum, \bar{k}_x versus \bar{k}_β , for the symmetric(-) and antisymmetric(--) SH modes of an infinite free plate (after Graff [7]).

$$(k_\beta h) = \left(\frac{n\pi}{2} \right)^2 + (k_x h)^2 \quad . \quad (2.49)$$

(2.49) is plotted in Figure 2-4 on axes again scaled by $2h/\pi$. Note in Figure 2-4 that all but the fundamental symmetric mode and all antisymmetric modes have cutoff frequencies given by

$$\omega = \frac{\beta \pi n}{2h} \quad , \quad (2.50)$$

below which modes become evanescent (imaginary horizontal wavenumber); however, the fundamental symmetric mode, $n=0$ in (2.49), is a nondispersive propagating wave independent of frequency. Since the cutoff frequency given by (2.50) is relatively high

for a typical arctic ice sheet (again, ~ 300 Hz in 3 meter ice), it is likely that only the fundamental symmetric SH mode will be of concern in this investigation.

2.1.2 Elastic Waves in a Floating Plate

The problem of a thin elastic plate over a liquid half-space differs from the free plate problem only in the boundary conditions at $z=h$. In place of (2.31), the boundary conditions are unchanged at the upper boundary with vacuum,

$$\tau_{xz_1} = \tau_{xy_1} = \tau_{yz_1} = 0, \quad z=-h, \quad (2.51)$$

but at the lower boundary they become

$$\tau_{xz_1} = \tau_{yz_1} = 0, \quad \tau_{zx_1} = \tau_{zx_2}, \quad u_{z_1} = u_{z_2}, \quad z=+h, \quad (2.52)$$

as is appropriate at a liquid/solid interface [7]. The subscript 1 refers to the plate and the subscript 2 the underlying liquid half space in (2.51), (2.52), and the work which follows.

Unfortunately, when the floating plate boundary conditions are used with equations (2.18) through (2.20) and (2.23), the new system of nine equations in nine unknowns cannot be analyzed as readily as the free plate system. The P and SV wave motions in the floating plate no longer reduce to purely symmetric and antisymmetric modes due to the presence of the liquid. Press and Ewing [12] studied the P and SV modes by making the simplifying assumption that $\lambda=\mu$, and derived an exact expression for the period equation,

$$P(2Q + \delta \cosh v_1 h \cosh v_1' h) + Q \delta \sinh v_1 h \sinh v_1' h = 0, \quad (2.53)$$

where

$$\delta = \rho_2 \alpha_2^2 (v_1'^2 - k_x^2) (v_2^2 - k_x^2) \frac{v_1}{\rho_1 \beta_1^2 v_2}$$

$$v = i k_{z\alpha}, \quad v' = i k_{z\beta}, \quad (2.54)$$

$$P = (v_1'^2 + k_x^2)^2 \cosh v_1 h \sinh v_1' h - 4 v_1 v_1' k_x^2 \sinh v_1 h \cosh v_1' h,$$

$$Q = (v_1'^2 + k_x^2)^2 \sinh v_1 h \cosh v_1' h - 4 v_1 v_1' k_x^2 \cosh v_1 h \sinh v_1' h.$$

Press and Ewing were further able to show that for long waves in a thin plate ($k_x h$ small), flexural waves analogous to the free plate's antisymmetric case exist and propagate with a period equation given by the approximation

$$\frac{c_f^2}{\beta_1^2} = \frac{8 \rho_1 (k_x h)^3}{3 \rho_2} \frac{1 - \frac{\beta_1^2}{\alpha_1^2}}{1 + \frac{2 \rho_1 k_x h}{\rho_2}}, \quad (2.55)$$

and analogous longitudinal (symmetric case) waves exist and propagate with a period equation given by the approximation

$$\frac{c_{lp}}{\beta_1} = 2 \left(1 - \frac{\beta_1^2}{\alpha_1^2} \right)^{\frac{1}{2}} \left\{ 1 + 2i(k_x h)^3 \frac{\beta_1 \rho_1}{\alpha_2 \rho_2} \left(1 - \frac{\beta_1^2}{\alpha_1^2} \right)^{\frac{1}{2}} \left[1 - \frac{4 \beta_1^2}{\alpha_1^2} \left(1 - \frac{\beta_1^2}{\alpha_1^2} \right) \right] \right\}. \quad (2.56)$$

Note in particular that the real part of the longitudinal wave velocity is unchanged from the free plate (2.39), but that the liquid half-space adds an imaginary part which represents attenuation proportional to the wavenumber cubed. In the short wavelength limit ($k_x h$ large), Press and Ewing showed that (2.53) produces Rayleigh waves on the free surface and Rayleigh and Stoneley (Scholte) waves at the ice/water interface. These interface waves are not important for the ice thicknesses and frequencies of concern in this work and will not be discussed further.

The change in boundary conditions is irrelevant to the SH wave, the derivation of which involves neither τ_{zz} nor u_z . The SH wave propagates unchanged in a plate regardless of the fluid (or vacuum) on the faces of the plate. Thus the solution for the SH modes in the floating plate is exactly that for the free plate discussed in the previous section.

2.2 Numerical Solutions

Numerical solutions to the transcendental characteristic equations for the floating plate have been obtained generally by making simplifying assumptions. As seen in the previous section, Press and Ewing assumed that the Lamé constants were equal and looked at the solution in the limit as the wavelength became very small or very large. A number of thin plate theories have been studied which model a fluid loaded plate in such a way as to account for only the lowest flexural and possibly longitudinal modes. Although Langley [13] has shown that the thin plate approximations can provide accurate results below the cutoff frequencies for the higher order symmetric and antisymmetric modes, with modern computing facilities and available tools these approximations are no longer necessary to achieve quick and accurate results from the exact equations. Stein [14] used a specialized computational routine to solve the P-SV system of equations for the floating plate numerically; however Schmidt [2] has developed a much more flexible tool to apply to this problem, the Seismo-Acoustic Fast Field Algorithm for Range-Independent environments (SAFARI).

2.2.1 Full Wavefield Global Matrix Solution

The SAFARI approach to solution of seismo-acoustic propagation in a horizontally-layered environment is at its heart an expansion of the techniques of solving

the depth-separated wave equation originally applied to acoustic propagation by Pekeris [15] and later extended to seismic propagation by Ewing, Jardetzky and Press [10]. To see how this technique works in SAFARI [3], the wave equation for compressional waves (2.5) is rewritten for a single horizontal layer in cylindrical coordinates with the assumption that the environment is axi-symmetric, range-independent (*i.e.*, two dimensional) and all sources are on the z -axis,

$$\left(\nabla^2 - \frac{1}{\alpha^2} \frac{\partial^2}{\partial t^2} \right) \phi(r, z, t) = f_s(z, t) \delta(r) \quad . \quad (2.57)$$

If the Fourier transform,

$$F(\omega) = \frac{1}{2\pi} \int_{-\infty}^{\infty} f(t) e^{-i\omega t} dt \quad , \quad (2.58)$$

and the Hankel transform,

$$G(k) = \int_0^{\infty} g(r) J_0(k_r r) r dr \quad , \quad (2.59)$$

are both applied to (2.57), the result is an ordinary differential equation in z only,

$$\left(\frac{d^2}{dz^2} - (k_r^2 - k_\alpha^2(z)) \right) \Phi(k_r, z, \omega) = \frac{F_s(z, \omega)}{2\pi} \quad , \quad (2.60)$$

where k_r is the horizontal wavenumber and $k_\alpha = \omega/\alpha$ as before. The solution to (2.60) is the depth-dependent Green's function, given at some radial frequency ω by

$$\begin{aligned} \bar{\Phi}(k_r, z) = \\ \Phi_p(k_r, z) + A^-(k_r) \Phi^-(k_r, z) + A^+(k_r) \Phi^+(k_r, z), \end{aligned} \quad (2.61)$$

where Φ_p is some particular solution to (2.60), Φ^- and Φ^+ are two independent solutions to the homogeneous form of (2.60), and A^- and A^+ are coefficients determined by the boundary conditions. If the z -dependence of k_α is restricted to cases for which (2.60)

can be solved analytically, then solution of (2.60) in a multi-layer system amounts to solving for the arbitrary coefficients of (2.61). If α is taken as constant and there are no sources, for instance, then solving for the depth-dependent Green's function yields

$$\Phi(k_r, z) = A^- e^{-ik_\alpha z} + A^+ e^{ik_\alpha z} , \quad (2.62)$$

and the potential is

$$\phi(r, z) = \int_0^\infty [A^- e^{-ik_\alpha z} + A^+ e^{ik_\alpha z}] J_0(k_r r) k_r dk_r . \quad (2.63)$$

For solid media, SAFARI takes β as constant (in each layer) and solves for $\bar{\Psi}(r, z)$ in a manner similar to that above; although as implemented in SAFARI the vector $\bar{\Psi}(r, z)$ is replaced by (in cylindrical coordinates) $\psi'(r, z) = \partial\psi_\theta/\partial r$. The equations for the displacements and stresses become

$$\begin{aligned} u_r(r, z) &= \frac{\partial}{\partial r} \phi(r, z) + \frac{\partial^2}{\partial r \partial z} \psi'(r, z) \\ u_z(r, z) &= \frac{\partial}{\partial z} \phi(r, z) - \frac{1}{r} \frac{\partial}{\partial r} r \frac{\partial}{\partial r} \psi'(r, z) , \end{aligned} \quad (2.64)$$

and

$$\begin{aligned} \tau_{zz}(r, z) &= (\lambda + 2\mu) \frac{\partial u_z}{\partial z} + \frac{\partial u_r}{\partial r} \\ \tau_{rz}(r, z) &= \mu \left(\frac{\partial u_r}{\partial z} + \frac{\partial u_z}{\partial r} \right) . \end{aligned} \quad (2.65)$$

Thus the depth-dependent Green's function is

$$\psi'(k_r, z) = B^- e^{-ik_\beta z} + B^+ e^{ik_\beta z} , \quad (2.66)$$

and the appropriate solution for the ψ' potential is

$$\psi'(r,z) = \int_0^\infty [B^- e^{-ik_z \beta z} + B^+ e^{ik_z \beta z}] J_0(k_r r) dk_r \quad (2.67)$$

Substituting (2.63) and (2.67) into (2.64) and (2.65) produces a set of four equations in the four unknown coefficients for the displacements,

$$\begin{aligned} u_r(r,z) &= \int_0^\infty \left[-k_r (A^- e^{-ik_z \alpha z} - A^+ e^{ik_z \alpha z}) \right. \\ &\quad \left. + ik_{z\beta} (B^- e^{-ik_z \beta z} - B^+ e^{ik_z \beta z}) \right] J_1(k_r r) k_r dk_r \\ u_z(r,z) &= \int_0^\infty \left[-ik_{z\alpha} (A^- e^{-ik_z \alpha z} - A^+ e^{ik_z \alpha z}) \right. \\ &\quad \left. + k_r (B^- e^{-ik_z \beta z} + B^+ e^{ik_z \beta z}) \right] J_0(k_r r) k_r dk_r, \end{aligned} \quad (2.68)$$

and the stresses,

$$\begin{aligned} \tau_{rz}(r,z) &= \mu \int_0^\infty \left[(2k_r^2 - k_\alpha^2) (A^- e^{-ik_z \alpha z} + A^+ e^{ik_z \alpha z}) \right. \\ &\quad \left. - 2ik_r k_{z\beta} (B^- e^{-ik_z \beta z} - B^+ e^{ik_z \beta z}) \right] J_0(k_r r) k_r dk_r \\ \tau_{rz}(r,z) &= \mu \int_0^\infty \left[2ik_r k_{z\alpha} (A^- e^{-ik_z \alpha z} - A^+ e^{ik_z \alpha z}) \right. \\ &\quad \left. + (2k_r^2 - k_\alpha^2) (B^- e^{-ik_z \beta z} + B^+ e^{ik_z \beta z}) \right] J_1(k_r r) k_r dk_r. \end{aligned} \quad (2.69)$$

This set of equations must be satisfied on both sides of each boundary between layers such that the boundary conditions appropriate to the adjacent layers (liquid/solid/vacuum) are satisfied. Since the boundary conditions must be satisfied at all ranges, the kernels of the integrals in (2.68) and (2.69) must also satisfy the boundary conditions, leading immediately to a linear system of equations in the unknown coefficients, A^- , A^+ , B^- and B^+ , at every horizontal wave number k_r .

In SAFARI the linear system of coefficients is solved numerically to determine the depth-dependent Green's functions at desired depths for a discrete set of wavenumbers; the set of wavenumbers chosen must be sufficient to allow the numerical determination of the inverse Hankel transforms in (2.68) and (2.69) for the desired ranges from source to receiver. The resulting transfer functions are determined at a

discrete set of frequencies, and again the set of frequencies chosen must be sufficient to support the numerical calculation of the inverse Fourier transform to determine the total response in the time domain. In principle, the SAFARI solution is exact, limited only by the accuracy of the numerical methods used to solve the linear systems and determine the inverse wavenumber and frequency transforms, and the need to describe the environment by discrete layers within which the wave equation is separable. Clearly, SAFARI must be applied with care and knowledge, in particular weighing the requirements of wavenumber and frequency sampling against the limitations of machine memory and processing time. For an investigator with a firm background in the fundamentals of wave propagation and numerical analysis, and with a little experience with the code, SAFARI is an ideal tool to apply to the problem of wave propagation in an elastic plate.

2.2.2 Attenuation

The treatment of elastic waves in a plate to this point has assumed frictionless propagation, but in reality some energy is lost due to internal friction with each cycle of stress. As developed in Aki and Richards [4], a dimensionless measure of this friction is

$$\frac{1}{Q(\omega)} = -\frac{\Delta E}{2\pi E} , \quad (2.70)$$

where E is the peak strain energy and $-\Delta E$ is the energy lost in each cycle. If attenuation is assumed to be a linear phenomenon, wave amplitude, A , is proportional to \sqrt{E} in a linearly elastic solid. If $Q \gg 1$ is also assumed, (2.70) can be rewritten

$$\frac{1}{Q(\omega)} = -\frac{1}{\pi} \frac{\Delta A}{A} . \quad (2.71)$$

For attenuation of a wave propagating in the x direction

$$\Delta A = \left(\frac{dA}{dx} \right) \lambda, \quad (2.72)$$

and (2.71) becomes

$$\frac{dA}{dX} = -\frac{\pi A}{Q(\omega)\lambda} = -\frac{1}{2} \frac{k_x A}{Q(\omega)}, \quad (2.73)$$

for which the solution is

$$A(x) = A_0 e^{\left(-\frac{k_x x}{2Q} \right)}. \quad (2.74)$$

This relation can be viewed as treating the wavenumber of a propagating wave as a complex value, *i.e.*,

$$k_x = k_x \left[1 - i \left(\frac{1}{2Q} \right) \right]. \quad (2.75)$$

The explicit assumptions of linearity used in the above development are made in the SAFARI code, and this approach to attenuation is adopted in this paper. It is common in ocean acoustics to express attenuation in dB/ λ , so that linear frequency-dependent attenuation is given by the parameter γ , where

$$\gamma = \frac{20\pi \log e}{Q}. \quad (2.76)$$

This convention is used in SAFARI and throughout this paper.

Chapter 3

Experimental Measurements

Before embarking upon detailed discussions of source location and inversion in later chapters, it is useful first to review the nature of the experimental measurements, both to understand the motivation for the chosen approach to propagation analysis (including the need for extensive work with localization of experimental sources) and to observe certain aspects of the measured wave forms which are in themselves astonishing. This chapter will first review the seismo-acoustic propagation experiments which generated the data used in later chapters and then will take a close look at the data collected, including the time series of longitudinal, flexural and SH mode waves generated by under-ice, underwater explosive charges.

3.1 The Experiments

All data sets included in this investigation were collected during experiments conducted during March and April 1987 at an ice camp designated PRUDEX, located in the Beaufort Sea approximately 100 nautical miles north of Prudhoe Bay, Alaska. The PRUDEX ice camp was established as a joint effort of the Woods Hole Oceanographic Institution, the Massachusetts Institute of Technology and the Polar Science Center of the University of Washington Applied Physics Laboratory with the primary objective of testing an Arctic Remote Autonomous Measurement Platform (ARAMP) data buoy [16]; however, other experiments were included in the program.

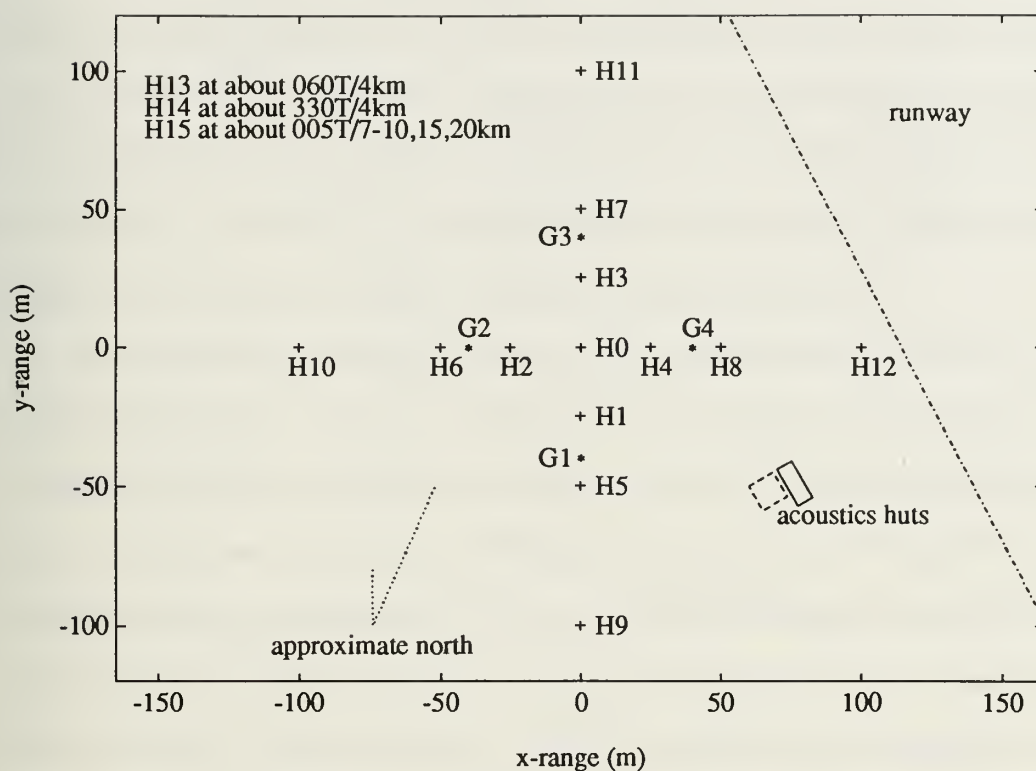


Figure 3-1: PRUDEX hydrophone and geophone array layout on the x/y plane used throughout this paper, hydrophones H0-H15 suspended at a 60 meter water depth, geophones G1-G4 frozen into the ice.

Originally intended only as engineering experiments designed to verify techniques and procedures for full scale experiments in later years, seismo-acoustic ice propagation experiments were conducted to observe the response of the PRUDEX ice canopy to underwater detonations. Preliminary review of the propagation data sets recorded during PRUDEX indicated that the data sets were of such high quality as to warrant a much more detailed investigation than had been planned when the sets were obtained.

Two co-located receiving arrays were used to record seismo-acoustic data at the PRUDEX camp. As shown in Figure 3-1, waterborne waves were received at a sixteen element hydrophone array. Each hydrophone was suspended at a depth of 60 meters at the locations shown. No exact hydrophone position data were available during the data

recordings of interest. Hydrophone response was sampled at 1000 Hz and recorded in digital form on an optical disk [17]. Waves propagating in the ice were received by an array of four 3-axis geophones. Geophones were frozen in the ice at the locations shown in Figure 3-1. The geophone data were recorded on wideband magnetic tape and later sampled at 1000 Hz and digitized by the author using the Woods Hole Oceanographic Institution's MIZEX Analog to Digital Converter [18].

Seismo-acoustic propagation data sets were generated during PRUDEX with a series of eight sets of underwater explosive detonations (shots), each set conducted in the early morning (Universal Time) on successive days in late March and early April. Each set of shots was conducted at a different location at ranges of from 300 to nearly 600 meters from the receiving arrays. Each set consisted generally of six separate shots conducted at source depths of 2, 4, 6, 8, 16 and 32 feet below the ice surface using various amounts of explosive charge. Table 3-1 summarizes the experimental shots conducted at the PRUDEX ice camp for which data were available. Of all shots completed, two shots in each of four data sets proved useful for the propagation analysis of this paper. Useful shots were primarily those which excited strong flexural and longitudinal waves in the ice, as well as producing a measurable geophone response to the waterborne acoustic wave generated by the detonation as the wave passed the ice beneath the geophone. The flexural waves were essential to the propagation analysis and inversion, while the longitudinal waves and the waterborne acoustic wave responses proved to be necessary for determining shot location. All of the required responses were generated by detonations at depths of 8 and 16 feet, at ranges of 500-600 meters, and using 1 or 2 feet of detonating cord (primacord) as the explosive source.

Because the propagation data sets were planned only to verify equipment and procedures and not with subsequent analysis in mind, much of the supporting

date	shot series	shot desig.	time (U.T.)	depth (feet)	charge
3/26/87	B	B2	0537:41	*	6 drams
		B3	0542:03	*	1 ft cord
		B4	0546:14	*	2 ft cord
3/27/87	C	C1	0418:37	*	4.5 drams
		C2	0419:58	*	6 drams
		C3	0423:29	*	1 ft cord
		C4	0427:24	*	2 ft cord
		C5	0436:00	*	4.5 drams
		C6	0438:51	*	6 drams
		C7	0442:36	*	1 ft cord
		C8	0445:33	*	2 ft cord
		C9	0456:34	*	4.5 drams
		C10	0458:06	*	6 drams
		C11	0501:54	*	1 ft cord
		C12	0504:29	*	2 ft cord
3/29/87	D	D1	0534:56	*	4.5 drams
		D2	0537:40	*	6 drams
		D3	0543:07	*	1 ft cord
		D4	0547:14	*	2 ft cord
3/31/87	F	F3	0546:21	*	1 ft cord
		F4	0550:48	*	2 ft cord
4/1/87	G	G1	0442:06	2	2 ft cord
		G2	0445:26	4	2 ft cord
		G3	0450:45	8	2 ft cord
		G4	0454:46	16	2 ft cord
4/2/87	H	H1	0548:25	64	2 ft cord
		H2	0553:28	32	2 ft cord
		H3	0557:14	16	2 ft cord
		H4	0601:15	8	2 ft cord
		H5	0604:39	4	2 ft cord
		H6	0606:44	2	2 ft cord
4/3/87	I	I1	0558:05	64	2 ft cord
		I2	0602:32	32	2 ft cord
		I3	0607:33	16	2 ft cord
		I4	0611:42	8	2 ft cord
		I5	0614:32	4	2 ft cord
		I6	0617:12	2	2 ft cord

Table 3-1: Summary of experimental shots recorded during PRUDEX propagation experiments. (*) indicates no depth recorded on shot log, "cord" refers to primacord, "drams" to explosive weight.

information which could have greatly simplified analysis was not recorded. Principal among the deficiencies in recorded data was that, except in only the most general terms, neither shot location nor shot time was recorded relative to the receiving arrays. As a result, a mandatory and non-trivial preliminary to detailed propagation analysis was locating each shot using only the seismo-acoustic data received at the arrays. A second deficiency was the failure to conduct a geophone calibration either before, during or after the experiment. Additionally, because the data from the two different arrays was recorded on completely different systems and no attempt was made to align the two systems precisely, the hydrophone time series could not be synchronized with the geophone time series before analysis began.

Further complicating the propagation analysis were known discontinuities in the ice canopy at PRUDEX; the explosive shots were made beneath the ice camp's runway, a relatively thin floe of new ice, while the receiving arrays were located on or below an abutting floe of thicker multi-year ice. Again, as detailed analysis was not anticipated, the surface geometry of the floe abutment was not surveyed, nor were any useful ice thickness or under-ice surveys conducted. In fact, the only available ice thickness data were recollections of the personnel who drilled ice holes in support of hydrophone array and under-ice shot placement. The runway was informally reported as being about one meter thick, and the array ice reported as being somewhat variable, about three meters in thickness.

3.2 The Observations

The purpose of this section is to review the time series observed during the PRUDEX propagation experiments and associate observed wave forms with the appropriate wave types discussed in Chapter 2. Additional characteristics of the

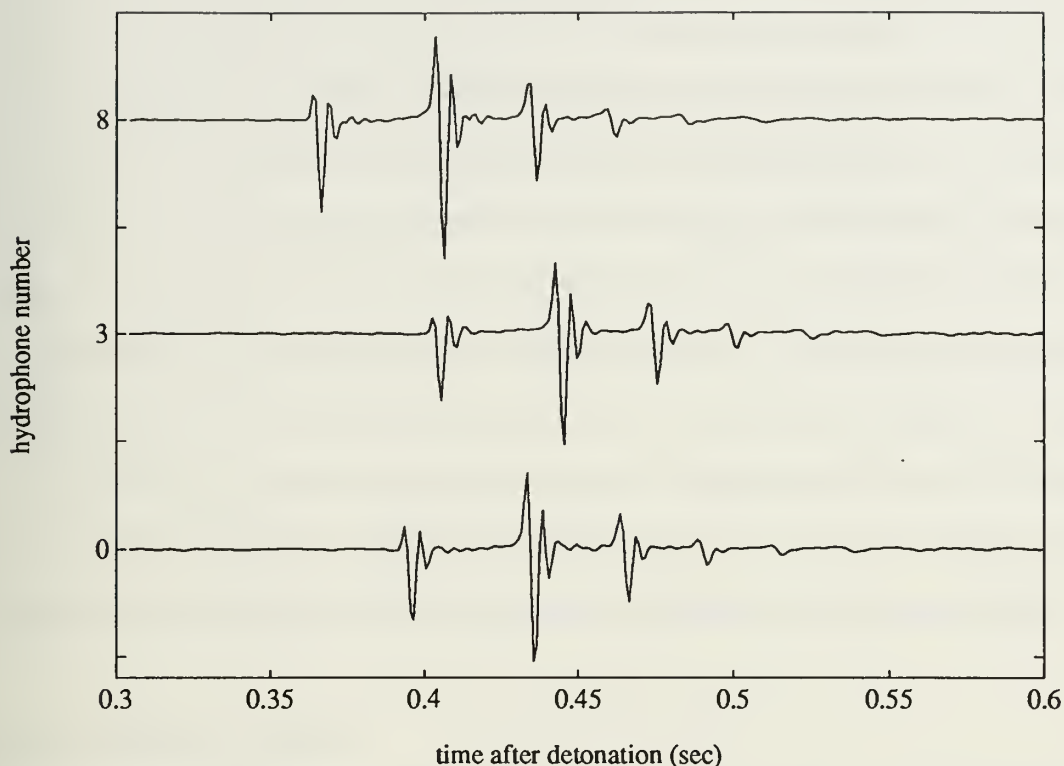


Figure 3-2: Waterborne acoustic waves as recorded at the output of PRUDEX array hydrophones (from top to bottom) #8, #3 and #0 in response to experimental under-ice shot number F3.

observed time series which greatly simplify analysis and inversion are identified and explained.

3.2.1 Hydrophone Data

Figure 3-2 shows a typical time series resulting from the detonation of 1 foot of primacord under the ice at a water depth of 8 feet and a range from array center of 570 meters, as recorded at the output of several PRUDEX array hydrophones. A striking feature of each of the traces in Figure 3-2 is the characteristic shock wave and bubble pulse pressure signature of an underwater explosive detonation. Bubble pulses, the pressure peaks which follow the initial detonation shock wave, result from successive

oscillations of the globular mass of gaseous materials that remains after the detonation is completed, each successive pulse being weaker than the preceding one as remaining energy is dissipated. Generally, only the first several bubble pulses are strong enough to be observable. Although the peak pressure of the first bubble pulse is about 40% that of the shock wave, at lower frequencies the energy density is actually higher in the first bubble pulse than in the shock wave. The principal peak in the combined spectrum of an underwater detonation occurs at a frequency of $1/T$, with T being the interval between shock wave and first bubble pulse [19]. As can be seen in Figure 3-2, after low pass filtering to prevent aliasing in the data acquisition system, the first bubble pulse is actually higher in amplitude than the shock wave due to its higher energy density at low frequencies. This characteristic is common to most shots analyzed.

3.2.2 Geophone Data

Geophones in the PRUDEX array were implanted in the ice with principal axes

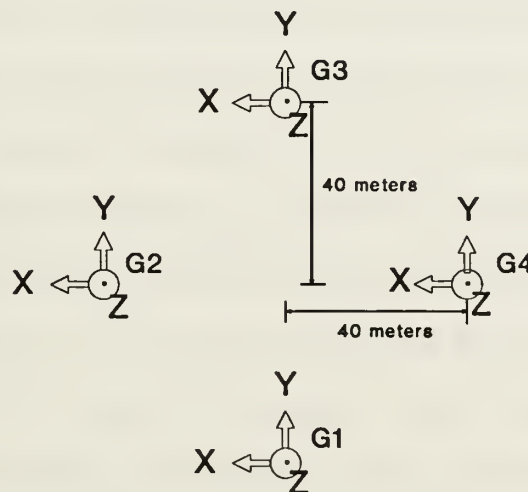


Figure 3-3: PRUDEX geophone array layout showing alignment of principal axes on each geophone.

aligned as shown in Figure 3-3; however, a much more useful aspect is obtained by resolving the output of the x and y axis geophones to axes corresponding to the radial and transverse directions relative to the propagation path of the appropriate shot. Figure 3-4 shows the time series corresponding to the same shot shown in Figure 3-2 as recorded at one 3-axis geophone and resolved to the direction of propagation.

The first arrival on the radial particle velocity trace in Figure 3-4 is the longitudinal plate wave, the pulse corresponding to the detonation shock wave arriving first followed by a larger one corresponding to the first bubble pulse. As the longitudinal wave is only slightly dispersive, the characteristics of the underwater detonation are retained in its time series; unfortunately later multiple arrivals generated due to complex interactions with discontinuities in the ice tend to confuse the pattern for the subsequent weaker bubble pulses. The longitudinal wave is also visible in the vertical geophone, although much less so than in the radial geophone, and later multiple arrivals dominate the time series until the flexural wave begins.

The flexural wave is the strongly dispersive wave beginning about 0.7 seconds after detonation in Figure 3-4 and continuing to the end of the trace. The flexural wave dominates the vertical geophone output, and is clearly visible in the radial geophone output. The dispersive nature of the flexural wave destroys the shock wave/bubble pulse characteristic of the response; however comparison with shots made at the same location but at different depths, hence with different bubble pulse intervals, shows that the flexural wave behaves as though its time of origin is the time of the first bubble pulse, not the initial shock. This correction is significant when determining the phase and group velocities of the flexural wave for comparison with theoretical results.

A second distinct set of pulses on the vertical geophone, arriving at about 0.4 seconds after detonation in Figure 3-4, correspond to the response of the ice plate by the

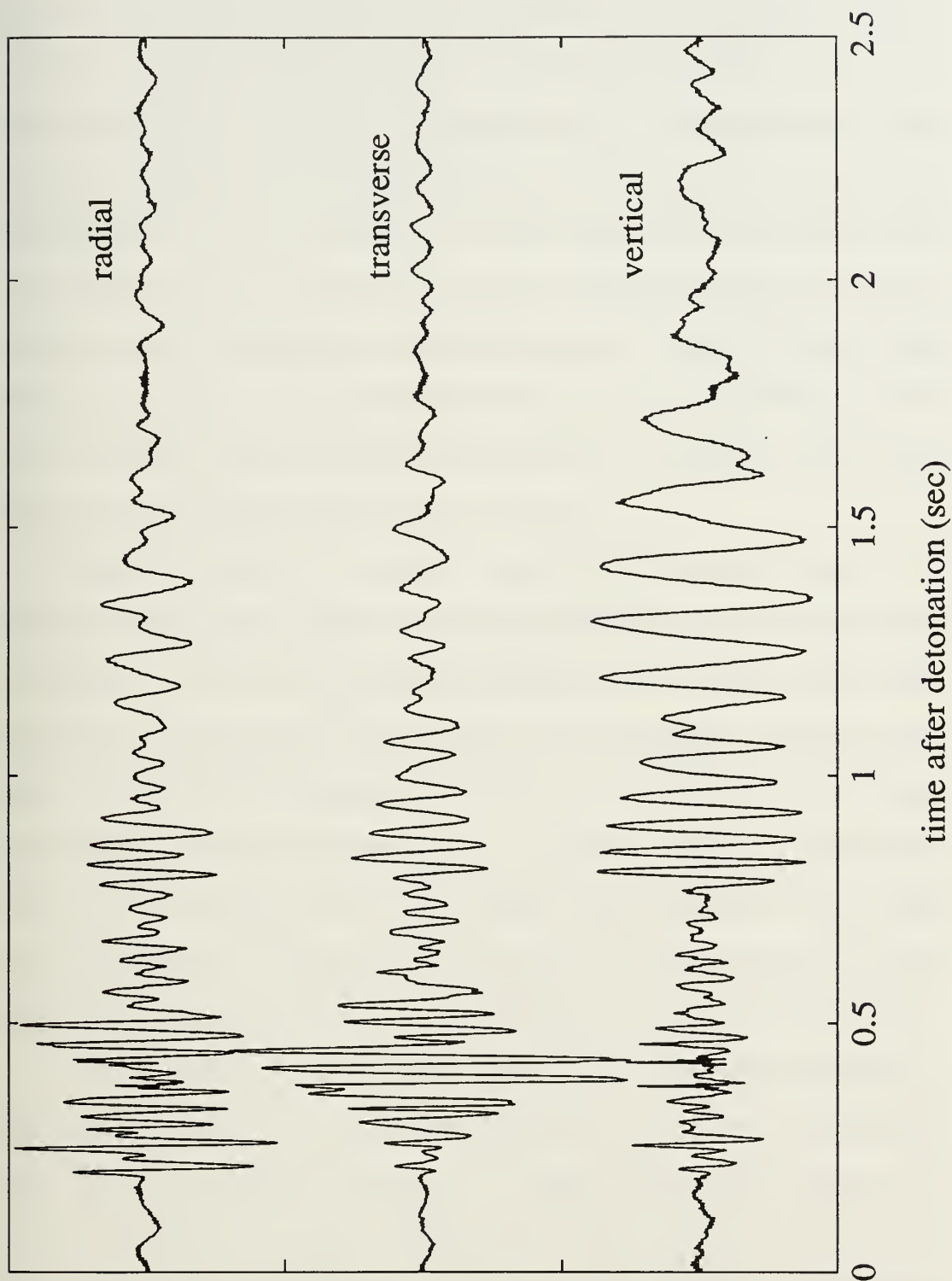


Figure 3-4: Time series as observed in the (top to bottom) radial, transverse and vertical directions on PRUDEX geophone #4 in response to experimental shot F3.

waterborne acoustic pulse arriving at the underside of the floe directly below the geophones. Since the travel path in the ice is short, the pulses replicate nearly exactly the characteristics of the hydrophone arrivals in Figure 3-2. At the liquid/solid interface the energy transmission is only in the direction of the normal to the surface, and the waterborne pulse is seen principally in the vertical geophone; although discontinuities in the underside of the ice produce a very small response in radial and transverse geophones as well. The responses to the waterborne pulse carry no information useful directly in the inversion for the elastic parameters of the ice; nonetheless, it will be shown in Chapter 4 that these pulses are indispensable to accurately determining the location of the experimental shots relative to the array.

Figure 3-5 contains two expanded plots for the vertical axis output of one geophone, with the response from two separate shots made at the same location overlaid for comparison. One shot was made using 1 foot of detonating cord at a depth of eight feet, and the other shot using 2 feet of cord at the same depth. The first plot in Figure 3-5 shows in detail the geophone response to the waterborne wave as it passes beneath the ice on which the geophone rests, as well as the change in the bubble pulse interval due to the change in the size of the charge. The second plot is of the flexural wave and demonstrates both the repeatability of the wave and the slight offset in the onset of the flexural wave introduced by the difference in the bubble pulse intervals.

Contrary to all expectations based on the theory of plate wave propagation, the largest amplitude response to an underwater detonation in each of the 3-axis geophones occurs only on the transverse geophone at a velocity corresponding roughly to the expected shear velocity in the ice. Further, the wave form of this transverse response retains generally the shock wave/bubble pulse characteristic of the source, indicating that this arrival is at most only slightly dispersive. The inescapable conclusion to be drawn

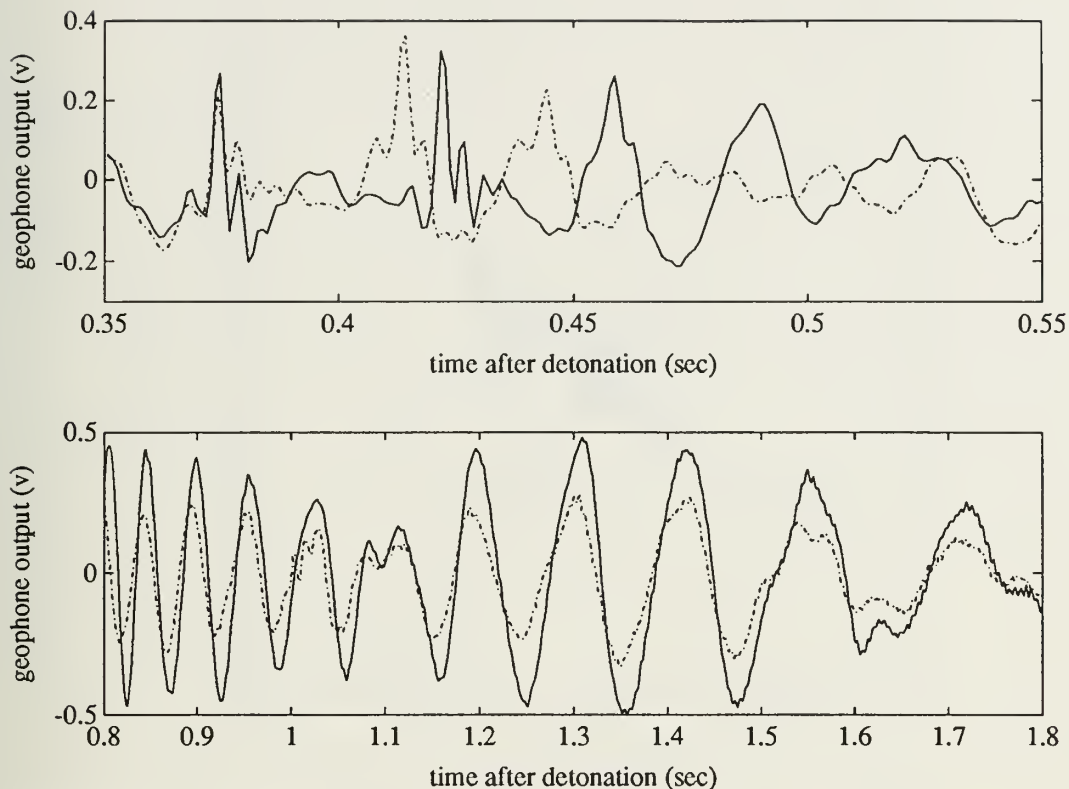


Figure 3-5: Vertical geophone #4 response for experimental shots F3(-·) and F4(-); top, the response to the waterborne acoustic wave as it passes under the ice, and bottom, the flexural wave.

from this combination of characteristics is that the largest amplitude wave propagating in the ice as a result of an under-ice, underwater detonation is the fundamental symmetric SH mode! This result is surprising because, as discussed in Chapter 2, there should be no interaction between SH waves in the plate and acoustic waves in the water; thus, an underwater detonation should not excite SH waves. Additionally, in a homogeneous, isotropic plate there is no mechanism to convert longitudinal and flexural (SV and P) waves into SH waves. Either the detonation does excite SH waves in a manner not understood, or out-of-plane scattering at discontinuities in the ice sheet provides a significant coupling between SH and SV/P modes. Either conclusion would be significant, in that most work in the arctic environment to date has ignored the SH

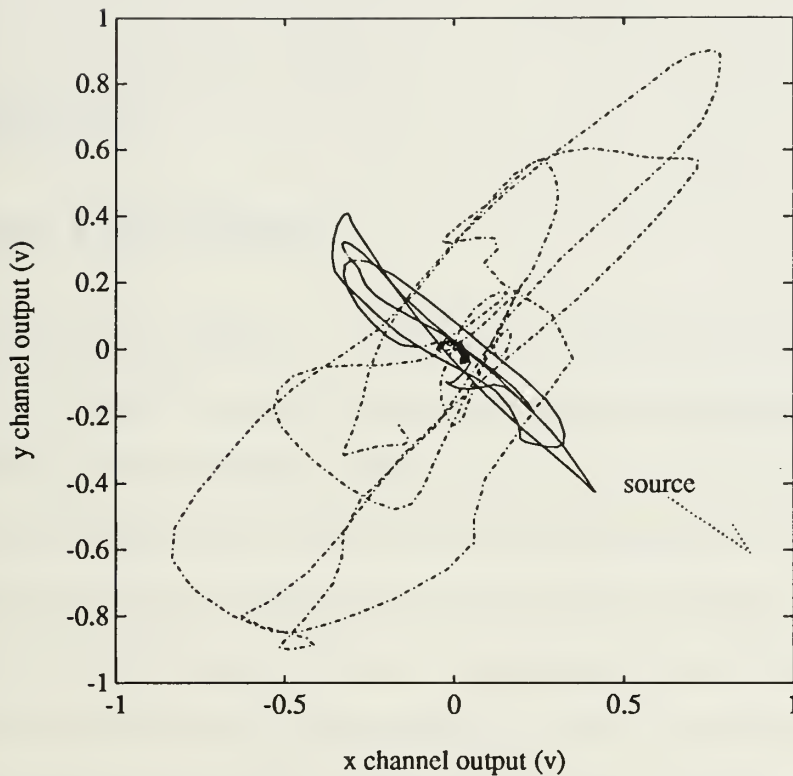


Figure 3-6: Hodograph for the x and y axes of geophone #3 showing the response to shot F4 at times from 0.1 to 0.323 seconds(-) and 0.323 to 0.5 seconds(-·-) after detonation.

mode in the ice as insignificant relative to ocean acoustics. The assumption that the SH mode may be safely discarded appears to be questionable based upon these observations.

Figure 3-6 shows a typical hodograph constructed from x and y geophone outputs during an under-ice shot. The hodograph further illustrates the clear radial polarization of the longitudinal wave arrival, followed by the equally clear transverse polarization of the later SH wave arrival. Similar geophone hodographs have been constructed during preliminary analysis of under-ice experimental detonations conducted in 1989 during the MIT/WHOI CEAREX ice camp [20], indicating that the appearance of SH waves in the PRUDEX data may not be an isolated phenomenon.

Chapter 4

Source Location

As discussed in Chapter 3, a critical part of the analysis of propagation data obtained at the PRUDEX ice camp is the two-dimensional localization of the under-ice explosive shots which excite seismo-acoustic propagation in the ice cover. Although the depth for these shots is known, only the most general information on their range and bearing from array center is available from records of the experiment.

Prior to commencing the analysis, it was believed that the information available from up to sixteen hydrophones could provide the basis for source localization, and that geophones at only four locations could contribute little of additional use. This predisposition to rely on the hydrophone data proved to be entirely erroneous, not only because analysis using the hydrophone data was insufficiently accurate, but also because it concealed information crucial to a thorough understanding of propagation in the ice.

This chapter reviews the data available to the localization effort and the routines used in localization, then examines the results for both hydrophone and geophone data. A detailed analysis of apparent anomalies observed in the geophone results leads to some unexpected conclusions about what these anomalies reveal about propagation in the PRUDEX ice cover. Finally, possible locations for the source of the SH waves noted in Chapter 3 are reviewed.

4.1 Localization Data

To take full advantage of the unique shock wave/bubble pulse character of both the received hydrophone and geophone data, the occurrence of each pulse series is identified in each received time series and associated with the appropriate non-dispersive wave type, *i.e.*, the longitudinal wave, the SH wave or the waterborne pulse response in the geophone data, or the waterborne wave in the hydrophone data. Times of each pulse maximum and minimum are interpolated to the nearest 0.1 msec. Thus, for each geophone time series the basic localization data consist of times of received maxima and minima at each of four geophone locations for the shock wave and the first several bubble pulses associated with each of three separate wave types. For each hydrophone time series, the localization data consist of the times of received maxima and minima for the shock wave and the first several bubble pulses at thirteen hydrophone locations (hydrophones 6, 9 and 12 in Figure 3-1 were not connected to the recording system).

The accuracy of the localization data so developed is effected by the limitations of the recording system and the interpolation routine, as well as by the presence, principally in the geophone data, of interfering waves. In order to estimate the uncertainty in the localization data, the hydrophone maxima are averaged to determine the mean time difference between a shot's shock wave and each of its bubble pulses. Since this bubble pulse Δt should be some constant value regardless of wave or receiver type, deviations from the mean value are used to develop the statistics of both hydrophone and geophone data so that an appropriate weight can be assigned in the localization routine.

A second key element of localization data is the sound speed in the first few meters of sea water directly beneath the ice. Fortunately, this data is readily available [16] for times within one hour of the shot times of interest. Figure 4-1 is a typical plot of temperature, salinity, and sound speed for the PRUDEX ice camp.

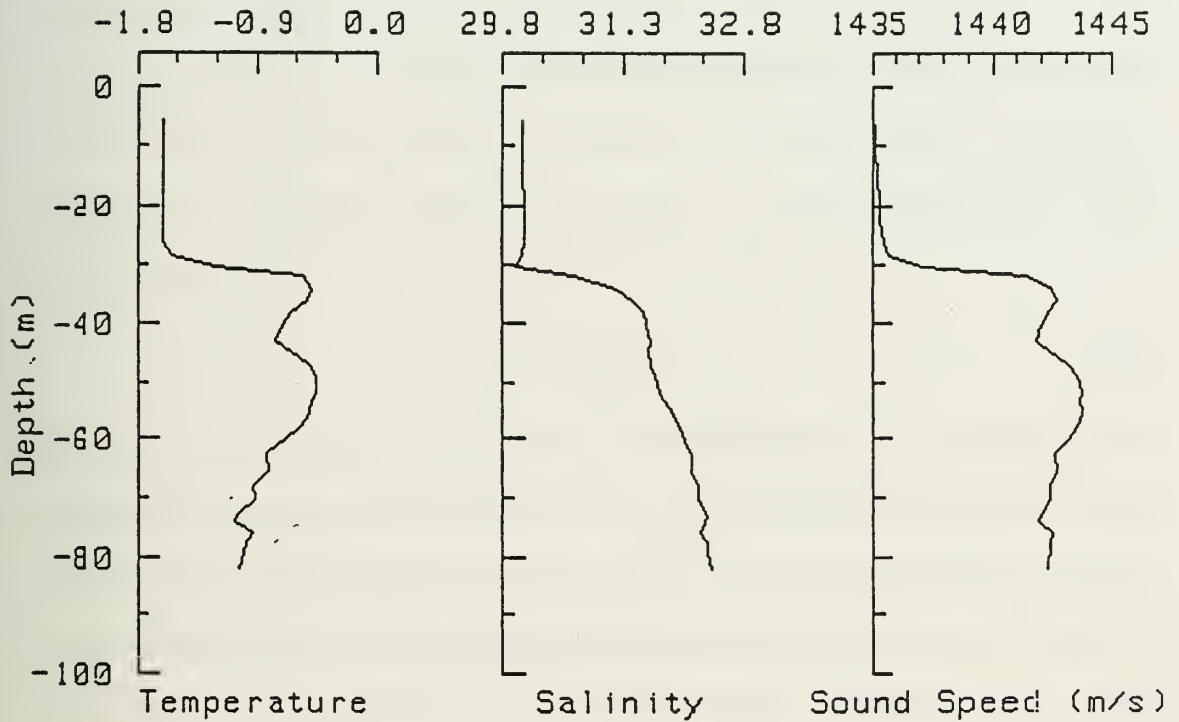


Figure 4-1: Temperature/Salinity/Sound Speed profiles at the PRUDEX ice camp, 31 March 1987, 0601 U.T. (from McPhee [16]).

Although not a major factor in the localization, the depth of each shot was recorded during testing. Informal discussions with personnel involved in the experiment indicate that these depth measurements were obtained by lowering the charges into the water on a marked line and are reliable values.

4.2 Localization Routine

To provide a flexible tool with which to localize each shot in the specialized ice

geometry, a FORTRAN computer routine centered around a singular value decomposition (SVD) routine adapted from Press, *et. al.*[21], is employed. SVD analysis provides a consistent method of combining data points from many different array elements, shots, and wave forms, while maintaining the ability to supply supporting parameters which might be known separately, such as wave speed and shot time, and the ability to specify the uncertainty in all data points and parameters individually. A system of equations is assembled in matrix form based on a simple linear relation for each pulse arrival at each array element,

$$t_j^i + r_a \left(\frac{1}{v_w} \right) = t_{jaw}^r \quad (4.1)$$

where t_j^i is the shot time for the j th shot, t_{jaw}^r the received time for a specific pulse of wave w at array element a from the j th shot, r_a is the assumed range from the shot to array element a (treated as a known value), and $1/v_w$ is the inverse speed of wave w . For example, a simple matrix system consisting of the shock waves from two different wave types (*e.g.*, the longitudinal wave and the SH wave), arriving from two separate shots conducted at a single location, and received at a two element array, becomes

$$\begin{bmatrix} 1 & 0 & r_1 & 0 \\ 1 & 0 & 0 & r_1 \\ 1 & 0 & r_2 & 0 \\ 1 & 0 & 0 & r_2 \\ 0 & 1 & r_1 & 0 \\ 0 & 1 & 0 & r_1 \\ 0 & 1 & r_2 & 0 \\ 0 & 1 & 0 & r_2 \end{bmatrix} \cdot \begin{bmatrix} t_1^i \\ t_2^i \\ \frac{1}{v_1} \\ \frac{1}{v_2} \end{bmatrix} = \begin{bmatrix} t_{111}^r \\ t_{112}^r \\ t_{121}^r \\ t_{122}^r \\ t_{211}^r \\ t_{212}^r \\ t_{221}^r \\ t_{222}^r \end{bmatrix} \quad (4.2)$$

or

$$A\vec{x}=\vec{b} \quad (4.3)$$

If one of the speeds or shot times is known, an additional row is appended to matrix A and vector b with this information. The system is then weighted by dividing each row of matrix A and vector b by the uncertainty of that row (making the reasonable assumption that the uncertainty in each equation is uncorrelated). For a given shot location, singular value decomposition solution of (4.2) after weighting yields the best fit to the data for shot time and wave speed. The uncertainty of each estimate is also available [21].

In order to locate a shot in space and time, the above SVD routine is employed in a matched field approach to search through two dimensional space for a best fit for shot times and wave velocities, as indicated by the lowest value of chi-square (χ^2), the sum of the square of the difference between the modelled array times and the data. The best fit corresponds to the most likely location for the shot. To evaluate the uncertainty in the best fit location, values of χ^2 are determined for each point in space searched by the localization routine, converted to dB, normalized to zero dB at the lowest value of χ^2 (i.e., converted to curves of $\Delta\chi^2$ from the best fit), and plotted. The best fit location and the estimated uncertainties (assumed to be Gaussian) are then used to compute a large number of Monte Carlo simulations of the data [21]. These Monte Carlo simulations are supplied to the localization routine and their best fit locations determined. Simultaneously plotting these best fit Monte Carlo-derived locations with the $\Delta\chi^2$ contours resulting from the original best fit allows a straightforward assignment of confidence limits to specific dB values of $\Delta\chi^2$.

4.3 Localization with Hydrophone Data

Although use of all available elements in the hydrophone array was intended, when localization using hydrophone data was initially attempted, it became immediately apparent that positions recorded for the elements located 100 meters and further from the array center were very inaccurate. Localization failed to converge meaningfully when data from these outer hydrophones were incorporated, and attempts to refine outer hydrophone positions with data from different shot locations on successive days failed due the small angular separation and long time interval between shot series. Limited thus to the inner 9 hydrophones (of which 8 were connected to the recording system) the localization routine proved very successful in refining shot bearing, but much less so in refining shot range.

Figure 4-2 is a plot of $\Delta\chi^2$ contours for a best fit shot location determined using hydrophone data, along with the best fit locations for 80 Monte Carlo simulations of that data. The 1 dB ellipse, corresponding to about a 90% confidence limit, has a major axis more than 900 meters long. With an estimated range from shot to array center of much less than this distance, wave velocities determined using travel times from the best fit shot location cannot be specified even to within $\pm 50\%$. As will be seen in the next chapter, inversion of ice propagation data is heavily dependent on measured wave velocities. Clearly, hydrophone-based shot locations do not provide the accuracy which reliable inversion requires.

4.4 Shot Location using Geophone Data

After having failed to determine a reliable location and time for any experimental shot using the hydrophone data, localization was begun using geophone data. With the geophone data it was hoped that the information carried in the multiple waves could offset the limitations of an array comprised of only four more closely spaced element

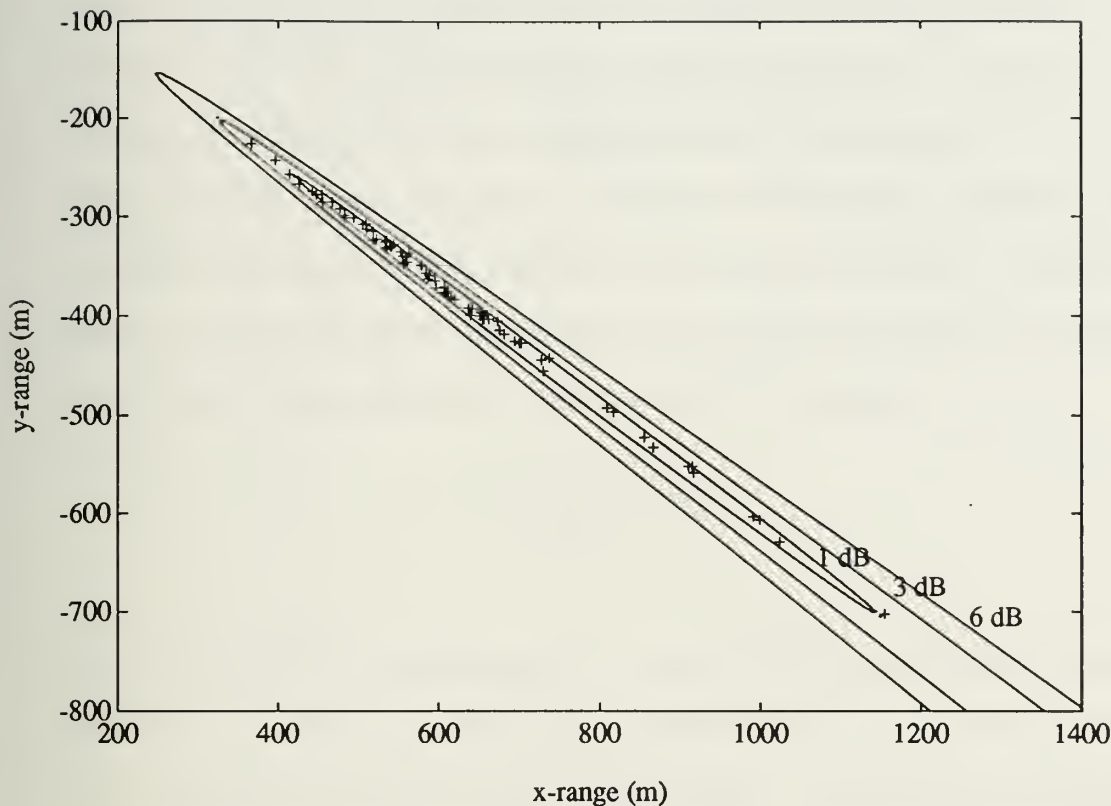


Figure 4-2: $\Delta\chi^2$ Contours for the best fit location for the F series of shots calculated using hydrophone array data, plotted with the best fit locations(+) for Monte Carlo simulations of that data.

positions. The results eventually much more than justified the expectations, but not until a thorough analysis and explanation of some apparent anomalies was completed.

4.4.1 Variations in Ice Thickness at the Receiving Array

The first anomaly is relatively easy to understand and eliminate. When only the arrivals of the response to the waterborne pulse are processed in the localization routine, the shot bearings correspond well with those produced by the hydrophone data, as is expected, but wave velocities are consistently reported as 10-15 m/s higher than the known value of about 1435 m/s. Since the relatively low uncertainty of the pulse measurements supports more accurate velocity determinations, some variation in the

travel path is postulated. Detailed numerical studies show that this problem is very likely due to variations in the ice thickness below each geophone - changes in pulse travel time of as little as 0.3 ms, as would be caused by a difference of 1 meter in ice thickness beneath different geophones, account for the velocity difference without significantly altering the bearing reported by the localization routine. To estimate the thickness at each geophone, ice thicknesses at the geophones are added as variables to the SVD system in the localization routine, so that (4.1) becomes

$$t_j^i + r_a \cdot \left(\frac{1}{v_w} \right) + \alpha \cdot 2h_a = t_{jaw}^r \quad (4.4)$$

where α is the (known) compressional wave velocity and $2h_a$ the unknown thickness at geophone a. To anchor the estimates, since the travel times are only weakly dependent upon ice thickness, thickness variables are also added as parameters and assigned the same average value and expected error. With this modification, the localization routine is applied to the existing best fit location and values for the geophone ice thicknesses determined. These values are then used to correct the received times, and the basic localization routine is used to determine a new best fit location. This location can be used recursively to determine new estimates of ice thickness and improve the best position; however, the process generally converges very rapidly. Final values for ice thickness at each geophone are shown in Table 4-1. Because the system is very sensitive to differences in thickness, but not to absolute thickness, only the differences from some average value are shown.

4.4.2 Evidence for Refracted Waves

Geophone Nr	Deviation from average thickness
1	+0.08 m
2	-0.18 m
3	-0.83 m
4	+0.97 m

Table 4-1: Deviations from the average ice thickness determined at each geophone in the PRUDEX array.

The basic version of the shot location routine utilizes only the two most clearly defined and essentially non-dispersive wave pulse arrivals at the geophone array, the longitudinal wave and the response to the impact of the waterborne pulse on the ice under the geophone. Inherent in the basic location routine is the assumption that the water and the ice plate are homogenous media, such that non-dispersive waves travel in straight lines at constant speed. As seen in Figure 4-1, this assumption is valid for the waterborne arrivals (except as noted above). For longitudinal waves traveling in the ice, however, the difficulties introduced by variations in ice thicknesses at the array foreshadow the final conclusion that the PRUDEX ice cover cannot be treated as a single homogeneous plate. When both waterborne and longitudinal waves are processed in the location routine, the resulting values are much higher than the apparent measurement uncertainty supports; however, most of this error lies in very poorly predicted arrival times for the longitudinal wave. Detailed review of solutions for all eight shots from four different locations discloses that in all cases the longitudinal wave discrepancy arises because the longitudinal waves are arriving from an apparent bearing about 8 to 10 degrees to the right of the waterborne pulses. A further review for any single shot location of the arrivals from all three wave types propagating in the ice

shows that each wave type is coming from a different apparent bearing than the waterborne pulse. Figure 4-3 is a plot of the apparent direction of wave arrival computed for each wave type from a single shot location. Assuming that all waves originate from the same point, Figure 4-3 strongly suggests a family of waves refracted in the horizontal plane.

Experimenters returning from the PRUDEX ice camp described a relatively straight ridge in the ice cover which marked the transition from the thin runway ice under which the experimental shots were made, to the thicker ice on which the receiving array was situated. This description, combined with the indications of refraction noted above, prompted an investigation into the possible existence of the horizontal refraction

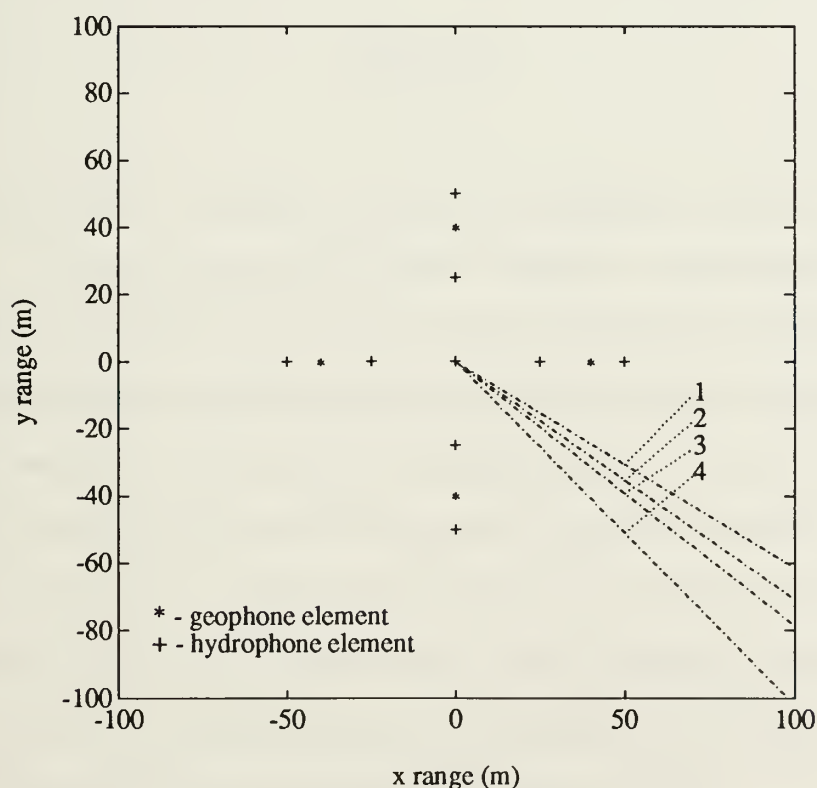


Figure 4-3: Plot of PRUDEX array layout showing apparent axis of arrival of (1) both the hydrophone and geophone water waves, (2) the SH wave, (3) the longitudinal wave, and (4) the flexural wave.

of waves propagating in the ice along a line created by a vertical plane separating the ice cover into two homogeneous half-plates of different thicknesses.

To investigate horizontal refraction, the location routine is further modified to determine, for a given index of refraction and ridge line orientation, the path which a wave travels from source to receiver. For refracted arrivals (4.1) becomes

$$t_j^i + r_{1a} \cdot \left(\frac{1}{v_{1w}} \right) + r_{2a} \cdot \left(\frac{1}{v_{2w}} \right) = t_{jaw}^r \quad (4.5)$$

where r_{1a} is the distance traveled in the first half-plate from the source to the ridge line on a path to array element a, r_{2a} is the distance traveled in the second half-plate from the ridge line to array element a, and v_{1w} and v_{2w} are the corresponding wave velocities in the two half-plates. Finally, adding an additional equation to the system,

$$\frac{1}{v_{1w}} - \frac{n}{v_{2w}} = 0 \quad (4.6)$$

where n is the index of refraction, establishes the appropriate ratio between the two velocities. In order to locate the most likely ridge line, a comprehensive search is conducted by computing for each shot the best fit shot location and corresponding value of χ^2 for a broad range of possible ridge line orientations and index of refractions. The most likely orientation is determined by combining the χ^2 values for all shots and choosing the orientation that produces the lowest χ^2 for all shots together. Figure 4-4 shows the $\Delta\chi^2$ contours for various values of the slope and y-intercept of the ridge line referenced to the array as an x/y plane with the origin at the center, and the positive x axis along the line containing geophone 4 and hydrophones 4, 8 and 12. Figure 4-5 shows the orientation of the best ridge line, described by the line

$$y = -1.95x + 223 \quad \text{meters} \quad (4.7)$$

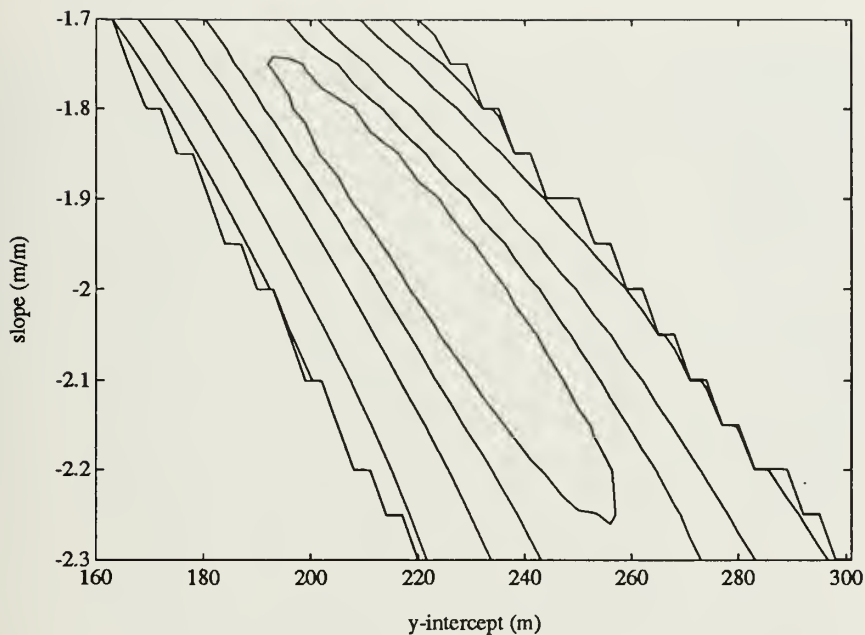


Figure 4-4: $\Delta\chi^2$ contours (in dB) for the best fit ridge line orientation, described by the line $y=mx+b$ on an x/y plane centered on the horizontal plane of the array with geophone #4 on the x -axis.

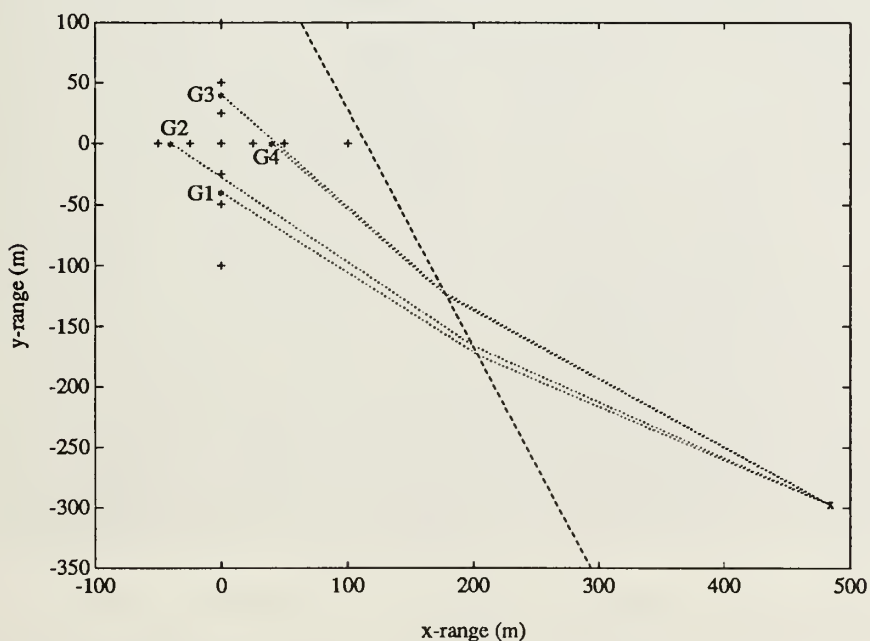


Figure 4-5: Plan showing on an x - y plane the PRUDEX geophone(*) and hydrophone(+) array, the best location for the F series of shots(x), the best fit ridge line(--), and the longitudinal wave paths from shot to each geophone(...).

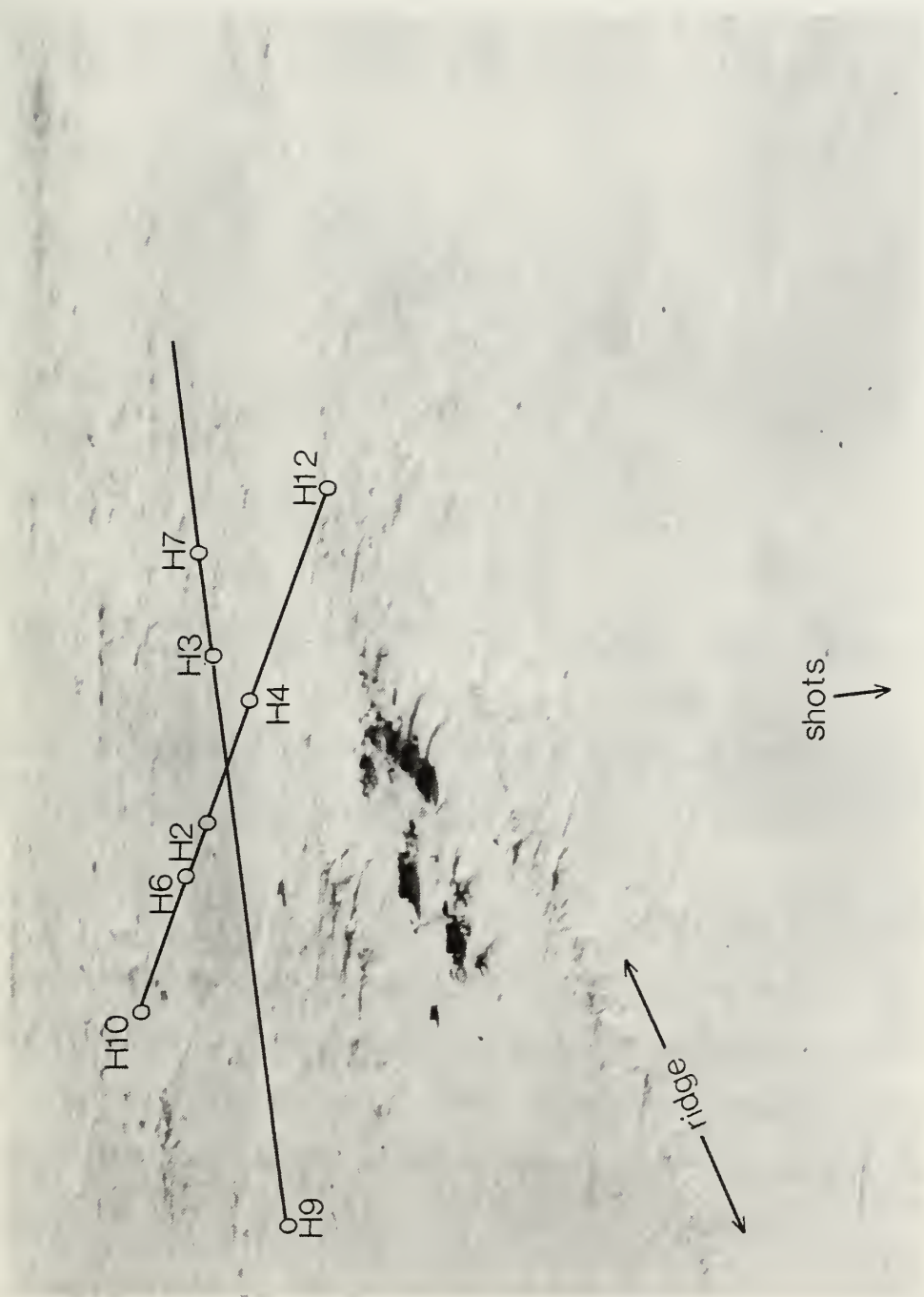


Figure 4-6: Aerial photograph of the PRUDEX ice camp and array, showing locations of identifiable hydrophones (geophones and some hydrophones are not visible), the array axes and the ice ridge line.

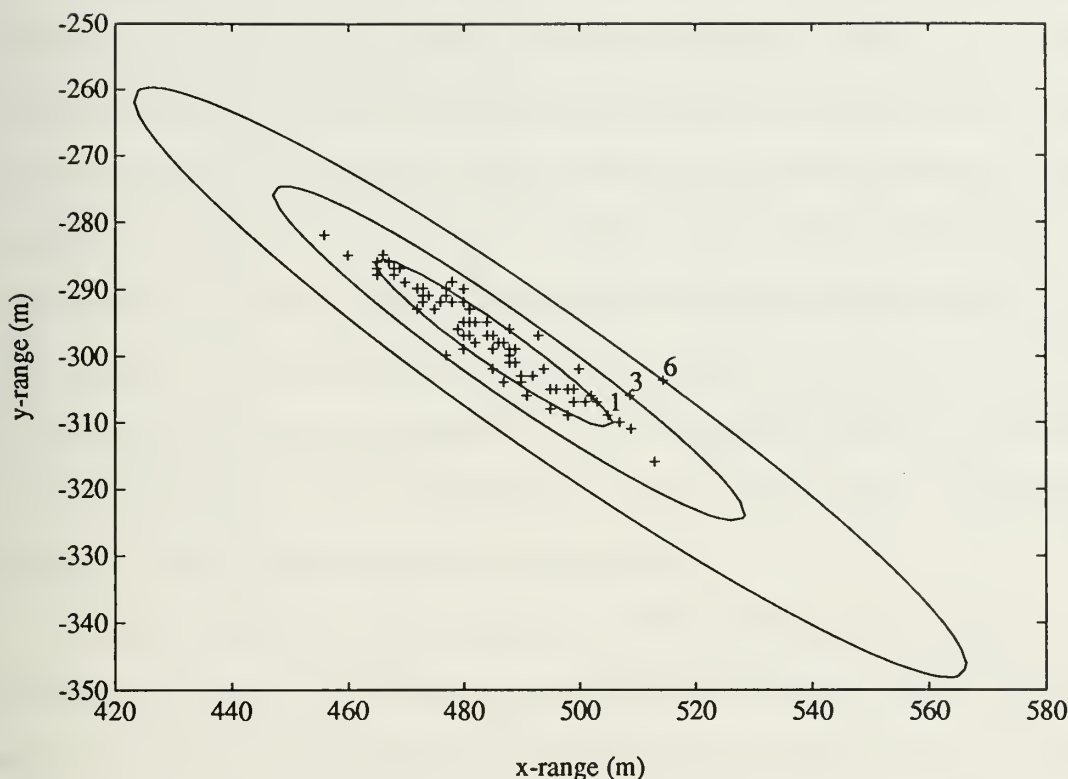


Figure 4-7: $\Delta\chi^2$ contours (in dB) for the best fit location for the F series of shots calculated using geophone data, plotted with the best fit locations for 80 Monte Carlo simulations(+) of that data.

relative to the array and the F series shot location. For any given shot series, the χ^2 value for the best fit refracted path is fully 6 dB better (lower) than the χ^2 value for the best fit to the same data on an unrefracted path. Figure 4-6 is the only available aerial photograph of the PRUDEX camp showing both the ridge line and the array layout. The best fit ridge line appears to correspond remarkably well with the ridge line in the photograph.

The search for the best ridge line necessarily includes as part of its operation the best fit location for all shots used in the search. Figure 4-7 is a plot similar to Figure 4-2 showing the $\Delta\chi^2$ contours for the best fit location for the F series shots, as well as the results of best fit searches of 80 Monte Carlo simulations of the received

data. The major axis of the 90% confidence limit ellipse (corresponding to the 1.6 dB contour) is only 60 meters long, implying an accuracy of about $\pm 5\%$ in wave velocities determined using this position. In fact, the slower velocities associated with the flexural wave will tend to be much more accurate than $\pm 5\%$, since the localization routine determines a corresponding shot time for which a wave traveling with the speed of sound in water (1435 m/s for these shots) will be measured exactly, regardless of the error in range. As a wave speed increases or decreases from this value, the speed measurement error increases accordingly. A wave traveling at 1000 m/s, for instance, will be measured at a range of 600 ± 30 m to within $\pm 1.6\%$, while a slower wave traveling at 500 m/s will be measured to within $\pm 3\%$.

Figure 4-8 provides a direct comparison of 90% confidence limit ellipses for the hydrophone and geophone based best fit locations for a shot series. While a system to monitor hydrophone positioning, a more sophisticated processing system, and a larger array can certainly improve hydrophone performance, it is remarkable that with all of these improvements, the performance of a hydrophone-based system will be unlikely to surpass that of a simple system of four 3-axis geophones.

4.5 Locating the Source of the SH Wave

The SH wave arrivals are investigated using the shot location routine in an attempt to determine their source and time of origin. Analyzing the SH wave arrivals separately, the range resolution is, as could be expected from the hydrophone results, very poor. Assuming the point of origin of the SH wave to be any given position between the shot and the ridge line, however, the best fit time of SH wave origin calculated by the location routine is roughly consistent with travel from the shot location to that point of origin at about the same speed as the SH wave's travel from the point

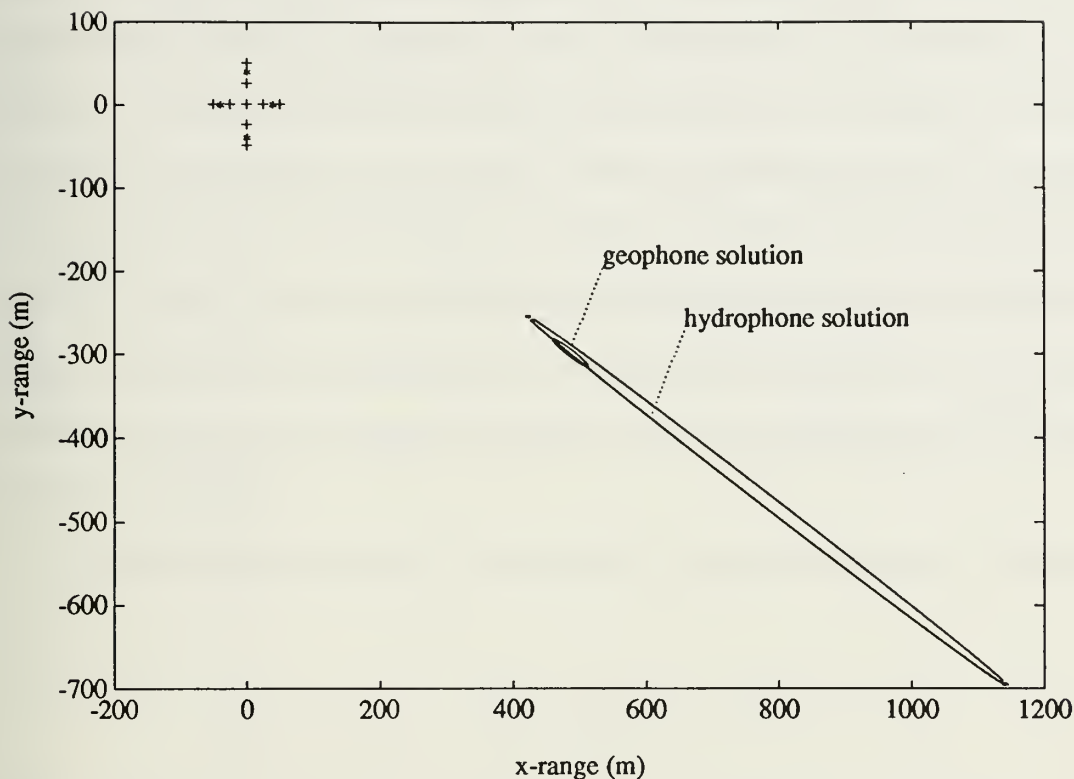


Figure 4-8: Plots of the 90% confidence limit ellipses for the F series shot location derived from geophone and hydrophone data.

of origin to the array; *i.e.*, the SH wave arrivals are consistent with generation by the shot itself, or with generation by the interaction of some wave traveling at about the same speed as the SH wave at some location near a line between the shot and the array.

Figure 4-9 is a plot of $\Delta\chi^2$ contours for the SH wave arrivals determined by restricting the time of origin to the shot time determined with the procedures of Section 4.4. The intersection of the 1 dB contours for the two locations demonstrates qualitatively the compatibility of the two solutions, and supports the argument that the SH wave is excited directly by the shot itself.

A second possible source for the SH wave is out-of-plane scattering during the interaction of the longitudinal wave with the ridge line. Figure 4-10 is a plot of $\Delta\chi^2$

contours for the SH wave arrivals calculated by constraining the time of origin to the average arrival time of the longitudinal waves at the ridge line en route from the shot to the array. The large offset of the center of the ellipse from the ridge line indicates that the SH wave arrivals are not consistent with their generation during the interaction of the longitudinal wave at the ridge line. Similarly, the flexural wave interacting at the ridge line is another possible mechanism for out-of-plane scattering and production of the SH wave; however, that possibility can be immediately dismissed as the SH waves arrive at the receiving array before the flexural waves (at the peak frequency of 20 Hz) arrive at the ridge line.

A fourth possible source is an interaction of the waterborne wave with some

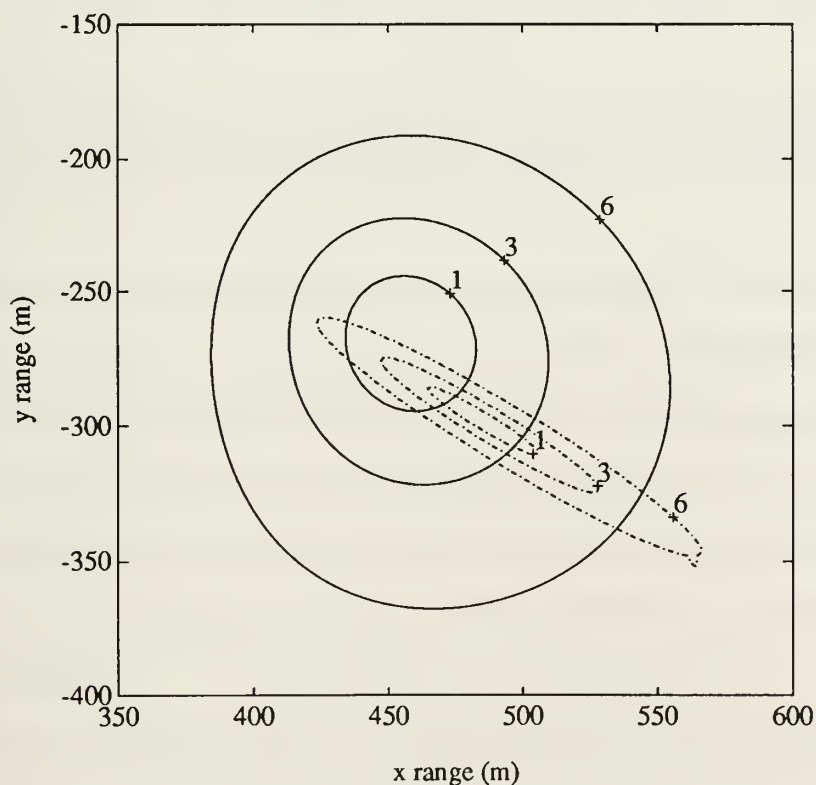


Figure 4-9: $\Delta\chi^2$ contours (in dB) generated by the shot location routine for the SH wave point of origin(-) assuming the time of origin is fixed at shot time, with contours for the best fit shot location(-) of section 4.4.

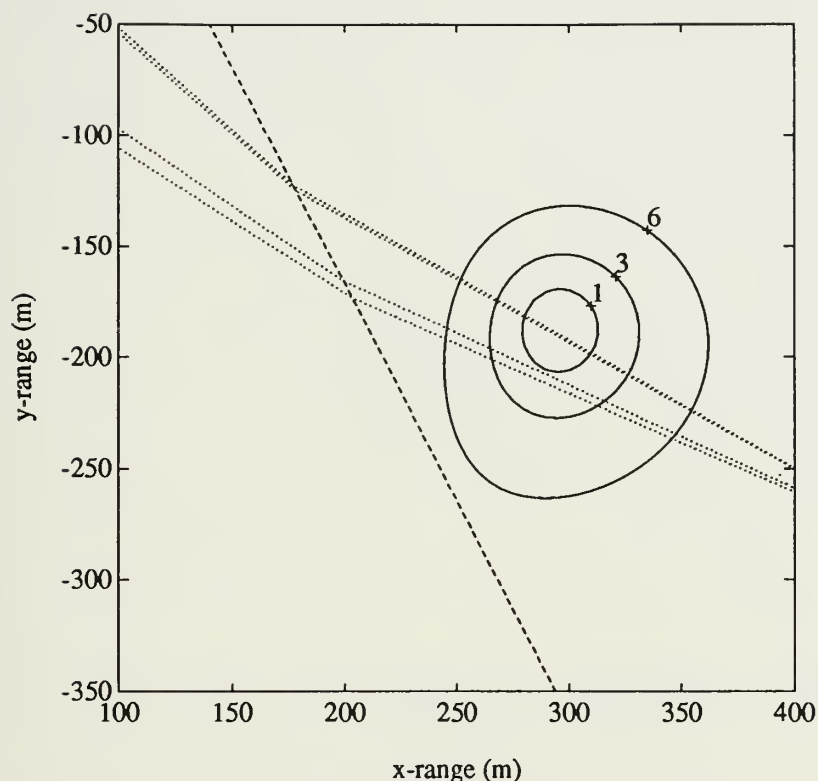


Figure 4-10: $\Delta\chi^2$ contours (in dB) generated by the shot location routine for the point of origin of the SH wave with time of origin fixed at the average time of longitudinal waves' arrival at the ridge line (···).

discontinuity on the underside of the ice. As the wave speed in water is comparable with that of the SH wave, this possibility cannot be ruled out immediately; however, Figure 4-11, the $\Delta\chi^2$ contours for the SH wave point of origin assuming that the SH wave time of origin coincides with the arrival of the waterborne wave at the ridge line, shows at least that the water wave/ridge line interaction is probably not the source, again because the location contours for the time of that interaction are offset relatively far from the ridge line.

Based on available evidence, the source of the SH wave cannot be positively identified. Origin at or near the shot location and time is consistent with the data. Interactions of the flexural wave, the longitudinal wave or the waterborne wave with the

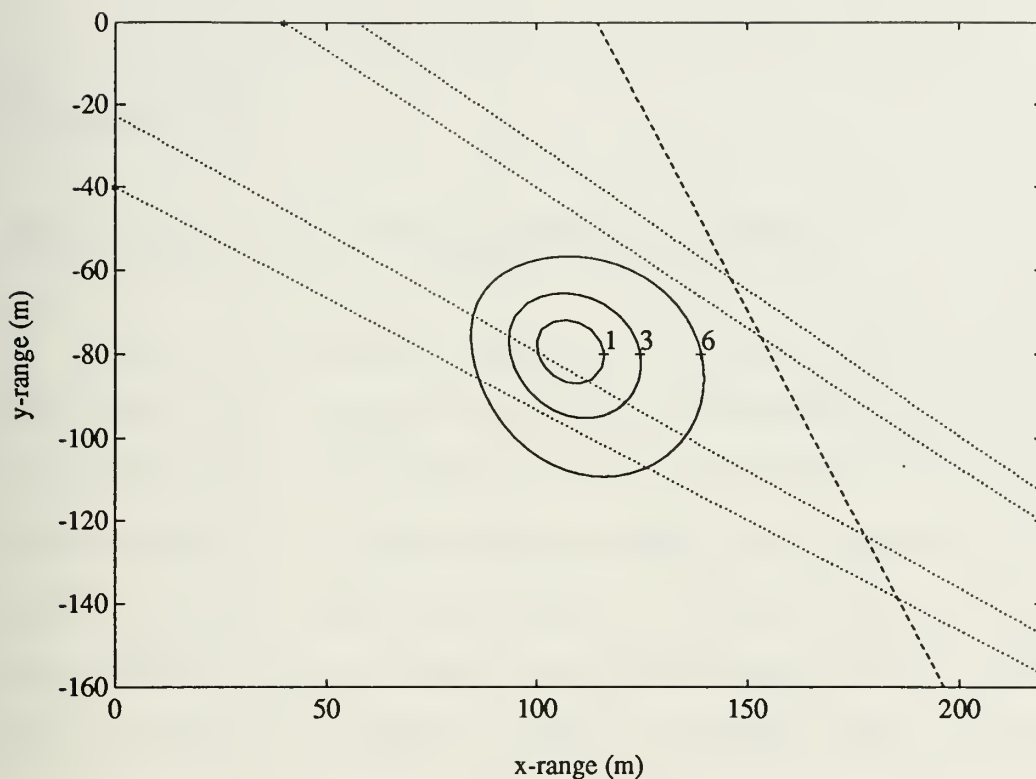


Figure 4-11: $\Delta\chi^2$ contours (in dB) generated by the location routine for the point of origin of the SH wave with the time origin fixed at the time of the waterborne waves'(...) arrival at the ridge line(--).

ridge line do not appear to be likely sources for the SH wave. Since the major known discontinuities in the PRUDEX ice canopy are associated with this ridge line, it is most likely that the SH wave is either excited directly by the under-ice detonation in an as yet unexplained manner, or it is generated by out-of-plane scattering in the immediate vicinity of the detonation, perhaps during interactions with some unknown feature on the underside of the ice canopy, in which case there is insufficient information in the PRUDEX experiment to determine which wave is the source.

Chapter 5

Inversion of Propagation Data

Solving the wave propagation problem in the manner of Section 2.1, computing particle motion based on the equations of motion, the characteristics of the material, a given geometry and a known excitation, is the forward problem in seismo-acoustics. Although solution of the forward problem is seldom easy, the approach is at least straightforward and the correct solution should be unique [7]. Taking the measured particle motions in response to a known source and processing that data "backwards" through the appropriate equations to obtain the unknown elastic and geometric parameters is the inverse problem. Inversion of seismo-acoustic data often becomes more complex than the comparable forward problem because it assumes solution of the forward problem as a starting point and must deal with non-unique solutions. A given set of elastic/geometric parameters will produce only one response to a given excitation; however, it is very possible that different sets of those parameters will produce the same measured response to that excitation. The likelihood of non-unique solutions to the inversion process necessarily increases as the number of unknown parameters increases.

5.1 Inversion Parameters

The principal parameters desired from the seismo-acoustic inversion can be seen by inspection of the equations of motion in a linearly elastic solid (2.1). The motion of ice particles, hence the propagation of waves in the ice, is dependent upon the ice

density ρ , and the ice Lamé constants μ and λ . Equivalently, using relations (2.6) and (2.7), the Lamé constants may be expressed as the compressional and shear velocities α and β .

Although not expressed directly in the equations of motion, internal friction in a propagating medium dissipates the energy of waves propagating in that medium. In most cases this attenuation must be known *a priori* or added to the list of parameters to be determined in the inversion. In this work attenuation is described by the two parameters γ_α and γ_β , the attenuation of compressional and shear waves, respectively, as described in Section 2.2.2.

Ideally, there are no unknown geometric factors to complicate an inversion. In this chapter shot location relative to the receiving array, as determined in Chapter 4, is considered a known value. The sparse information available about ice thickness in the vicinity of the PRUDEX ice camp necessitates treating ice thickness as an unknown and including it in the inversion.

5.2 Previous Measurements

Although the mechanical properties of sea ice have been extensively studied [22], very little work has been done to determine the low frequency elastic properties of the arctic ice cover *in situ*. Until recently, actual measurements have been limited to some early wave speed measurements in freshwater lake ice [5] [6] [23], and pack ice [24] [25], high frequency attenuation measurements in glacial ice [26] [27] and sea ice [28], wave speed profiling in both lake and sea ice [29], and data obtained from small scale laboratory experiments. As a result, determinations of the low frequency properties of arctic sea ice were largely inferred from other ice environments or extrapolated from high frequency laboratory and *in situ* data. As an excellent

example of this approach, McCammon and McDaniel [22] have employed a comprehensive summary of available laboratory and field measurements to determine values for the attenuation in the arctic sea ice, for use in studies of the acoustic reflectivity of the ice cover. Based on this summary, they have estimated that compressional wave attenuation can be approximated by

$$\gamma_{\alpha} = 6 \cdot 10^{-5} \cdot \alpha \frac{dB}{\lambda} \quad (5.1)$$

and (assuming Poisson's ratio to be constant at 0.33) shear wave attenuation by

$$\gamma_{\beta} = 3.6 \cdot 10^{-4} \cdot \beta \frac{dB}{\lambda} . \quad (5.2)$$

Results obtained by such a combination of extrapolation and inference may accurately represent the characteristics of seismo-acoustic propagation at high frequencies, but it is questionable whether these values may be translated to reflect low frequency behavior as well. At low frequencies and long wavelengths, macroscopic discontinuities, such as cracks and ridges in an arctic ice plate, may reduce propagation speed and increase attenuation in the medium.

Recently, several investigators have obtained values for the elastic parameters of arctic ice at low frequencies. In 1986 Stein [14][30], as an adjunct to other studies, estimated values for shear and compressional velocities and attenuations from earlier work at two arctic sites. In 1989 Brooke and Ozard [31] completed a detailed study of the elastic properties of sea ice based on measurements in the Slidre Fjord of the Canadian Archipelago in 1986 and 1987. The results of Stein, and Brooke and Ozard are summarized in Table 5-1.

5.3 The Inversion Procedure

	Stein	Brooke and Ozard			
		Smooth Ice		Rough Ice	
data date	1980-82	1987	1986	1987	1986
α m/s	3500	NA	NA	NA	NA
c_{lp} m/s	NA	3084	2960	2893	2864
β m/s	1800	1705	1891	1660	1746
γ_α dB/ λ	0.46	NA	NA	NA	NA
γ_β dB/ λ	1.57	20-40Hz	0.32	0.45	2.33
		40-80Hz	1.00	0.57	2.55
		80-120Hz	0.38	0.49	1.33

Table 5-1: Summary of recent measurements of the elastic parameters of arctic sea ice at low frequency.

Inversion of the PRUDEX propagation data is conducted initially with the assumption that the floating ice canopy between source and receiver can be treated as a single homogeneous plate, and that only the longitudinal and flexural waves are excited by the explosive charge. Although neither of these assumptions is actually valid, the methods of this procedure serve to demonstrate the power of SAFARI modeling, and the results can be viewed as a form of "average" behavior. The inversion is then revised to reflect the more complete knowledge of the plate's character obtained in Chapter 4.

5.3.1 Inversion for an Infinite, Homogeneous Plate

A straightforward way to simplify a seismo-acoustic inversion is to select a small subset of the full set of elastic parameters describing the propagating media, and isolate for study a portion of the measured response which is sensitive only to the elements of

this subset. Preliminary study of the sensitivity of the flexural wave in a floating ice plate to variations in the elastic parameters shows that the flexural wave is relatively insensitive to variations in both the compressional wave velocity and the density of the ice. Because of the insensitivity to the density of ice, a nominal value of $.91 \text{ gm/cm}^3$ [32] is used throughout this work, and no attempt is made to determine ice density in any inversion. More importantly, this study shows that the flexural wave is dependent only upon the shear velocity, the attenuation values, and the thickness of the ice - it can be isolated to invert only for this more limited number of parameters. In addition, the dispersion curve of the flexural wave, *i.e.*, the relation of the flexural wave's group velocity to its frequency, is essentially independent of attenuation, and the measured dispersion curve can be inverted for only the shear velocity and the ice thickness.

Adopting an approach similar to that used by Jensen and Schmidt [33] to determine shear speed and shear attenuation of the sea bed from analogous Scholte wave data, the first step in the inversion consists of constructing a dispersion curve for the flexural wave. The dispersion curve is developed using the flexural wave responses and the positions determined for the eight experimental shots which not only excited a vigorous flexural wave, but also excited observable longitudinal waves and responses to the waterborne pulse (necessary for localization). In this section the positions used are those determined by treating the ice sheet as a homogeneous plate. The dispersion curve is built by applying a moving Fourier transform with a Hanning window to the time series, with the necessary window size determined by the simple expedient of increasing its length until the dispersion curve is stabilized [34]. All thirty-two individual curves (eight shots received at four vertical geophones) are then normalized to a constant noise value and combined to produce a single best dispersion curve for the

assumed homogeneous ice plate.

Having obtained an experimental dispersion curve, the inversion proceeds by selecting a likely model for the unknown parameters, using the SAFARI numerical modeling routine to determine a synthetic dispersion curve, comparing the model and the experimental dispersion curves, developing a correction to the model, and recursively refining the model until the model's curve converges with the observed one. If the ice thickness is known, the above procedure will quickly determine the correct shear velocity; unfortunately, the ice thickness at the PRUDEX ice camp is not known. For any given thickness and shear velocity, a family of solutions are found which can reproduce the same flexural wave velocity at a given frequency simply by adjusting the ice thickness up or down and compensating with an appropriate change in shear velocity. While some difference does arise between two such similar solutions over the frequency range of interest (2-60Hz), this difference is well within the accuracy available in comparing dispersion curves. This problem is illustrated in Figure 5-1, which shows several families of dispersion curves calculated for two different shear velocities and various ice thickness values.

The uncertainty in shear velocity is largely eliminated by expanding the inversion to include the longitudinal wave. As the longitudinal wave is essentially non-dispersive, this expansion necessitates a shift to the time domain and a direct comparison of experimental and synthetic time series. In addition to providing the compressional wave velocity, this expansion has the added benefit of allowing the estimation of the compressional and shear wave attenuation as well. The longitudinal wave is largely insensitive to ice thickness, casting some doubt on its ability to diminish the uncertainty in the shear velocity; however, it is so sensitive to shear velocity that only a very limited range of shear velocities can combine with a reasonable compressional wave

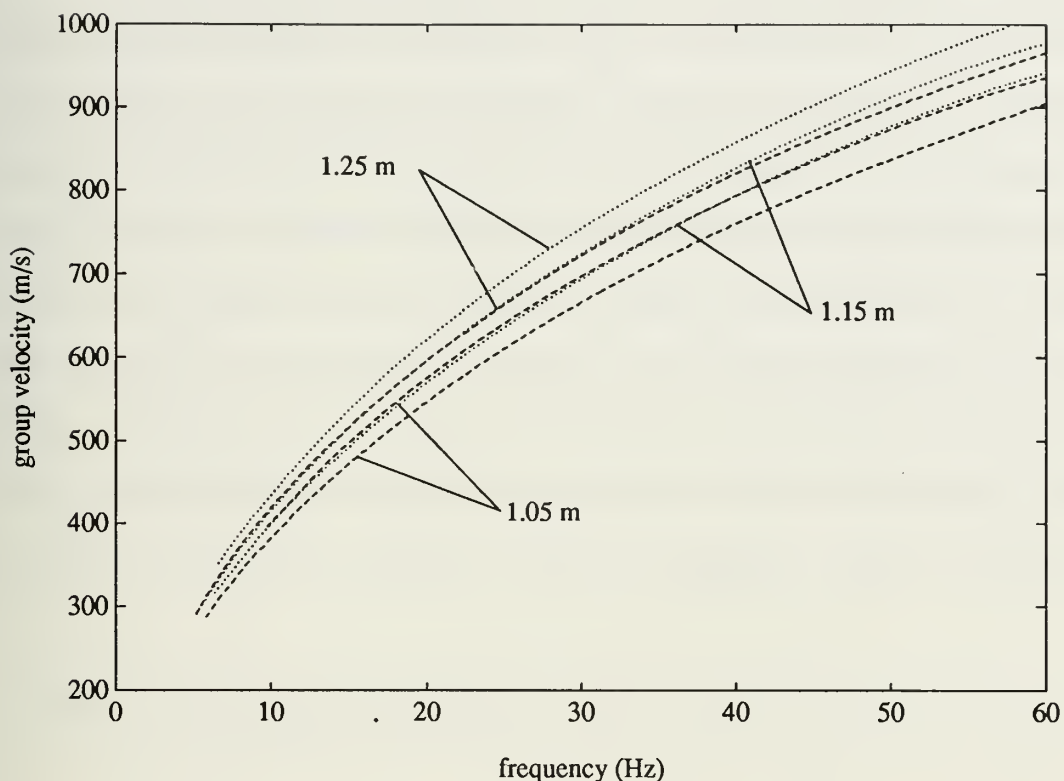


Figure 5-1: Two sets of dispersion curves for flexural waves in ice at shear velocities $\beta=1600\text{m/s}$ (--) and $\beta=1800\text{m/s}$ (...), and (top to bottom in each set) ice thicknesses of 1.25, 1.15 and 1.05m.

velocity to match the observed longitudinal wave. Figure 5-2 illustrates the dependence of the longitudinal wave on shear and compressional velocities, as well as demonstrating its essentially non-dispersive nature. Of equal importance in reducing the uncertainty in the uniqueness of the inversion, matching the observed flexural wave in the time domain is more sensitive to errors in flexural velocity over a wide frequency range than matching the calculated and observed dispersion curves.

A complication introduced by the decision to shift to comparing synthetic and observed time series is the necessity to provide an accurate representation of the explosive source used to excite the observed waves. A computer routine based on equations provided by Wakeley [35] has proven to be very successful in reproducing

the acoustic pressure signature measured at 1 meter from a known underwater explosive source; although possibly due to the effect of the extreme cold on the explosives, the bubble pulse intervals predicted by Wakeley's routines are consistently longer than observed at PRUDEX for the same explosive weight and depth. This discrepancy is resolved by reducing either the explosive weight or the proportionality constant used in the equations slightly from that provided by explosive tables [36][37] for a given length of primacord or dram weight of explosive, such that the synthetic and observed bubble pulse intervals agree. In this way the relative spectrum levels of the real and synthetic shots are identical. It is likely that the absolute levels are also equal, but there is insufficient information available to verify this assumption. Figure 5-3 shows the

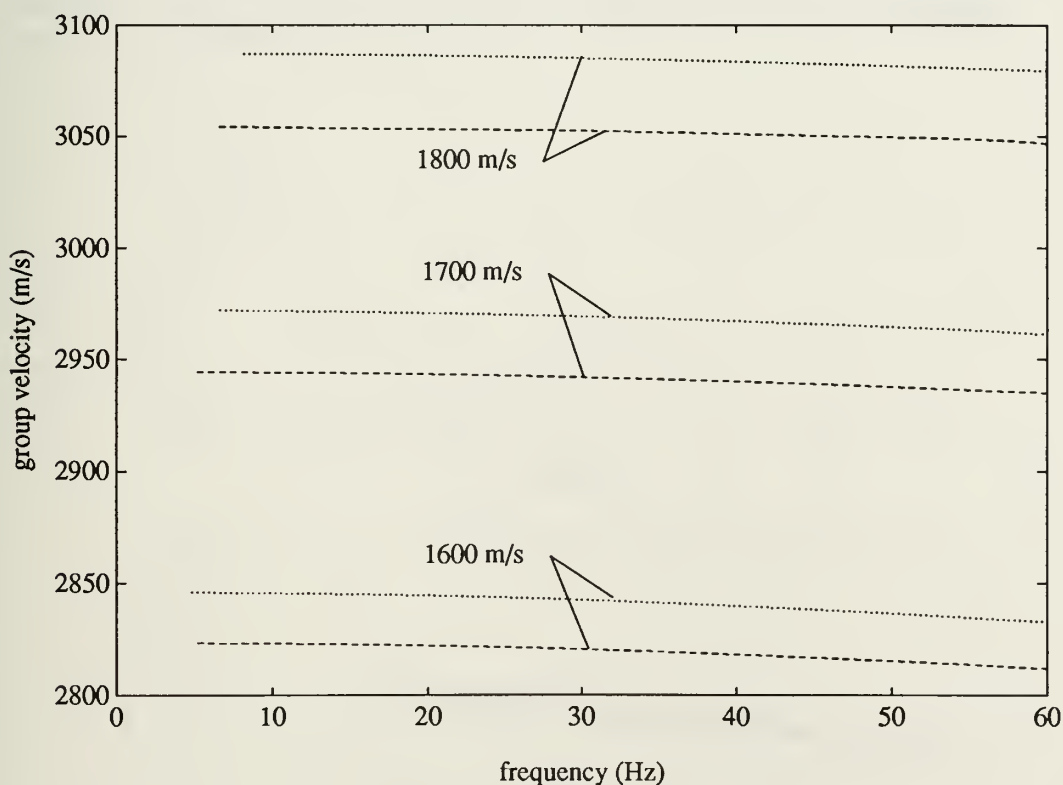


Figure 5-2: Two sets of group velocity curves for longitudinal waves in ice with compressional velocities of 3500m/s(...) and 3400m/s(--) and shear velocities (top to bottom in each set) of 1800, 1700 and 1600 m/s.

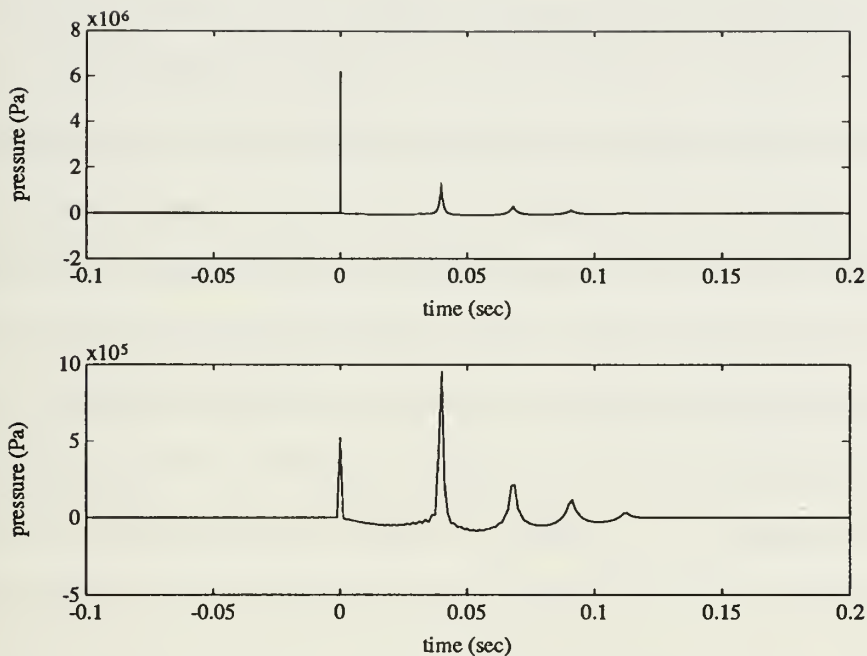


Figure 5-3: Synthetic time series for the pressure signature at 1 meter for an explosive charge simulating shot F3; top, sampled at 10 KHz, and bottom, prefiltered and decimated to 1000 Hz.

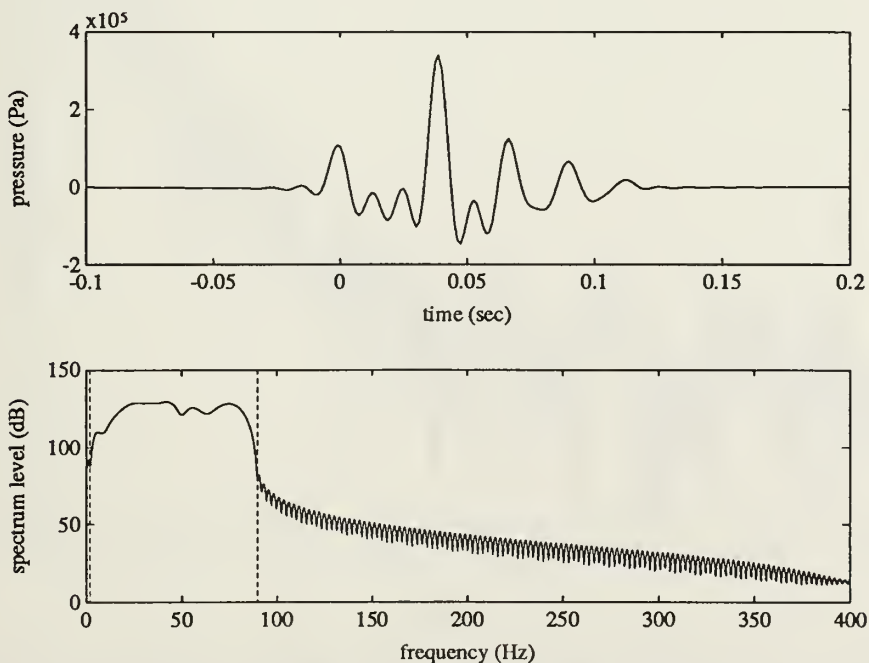


Figure 5-4: Top, synthetic time series of Figure 5-3 filtered to a 2-90 Hz band, and bottom, spectrum of filtered time series.

synthetic pressure signature of the explosive charge (1 foot of primacord) used in shot 3 of series F. Note that after prefiltering and decimation to a sample rate of 1000 Hz the first bubble pulse is larger in both amplitude and energy content than the initial shock wave, duplicating the relation seen in the experimental pulse trains. One of the requirements of the SAFARI pulse calculation routine is that to avoid "ringing" in the output time series, the frequency integration routine must be truncated where the source pulse has a frequency minimum [3]. To meet this requirement, as well as to limit the computation required for the frequency integration, the source pulse is digitally filtered [38][39] to a 2-90 Hz band, as shown in Figure 5-4. Limiting the frequency integration to this band has no effect on the inversion. The partial spectrum of a typical

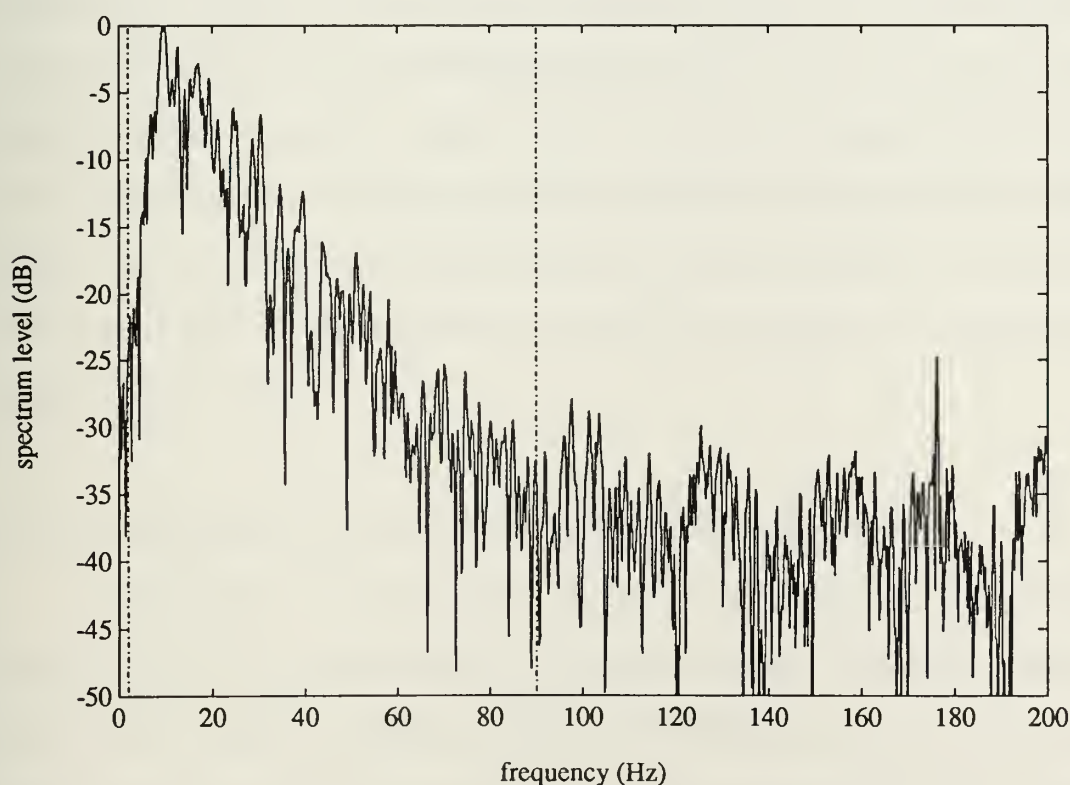


Figure 5-5: Spectrum of signal received on vertical component of geophone #3 during experimental shot F3, showing preponderance of energy in the 2-90 Hz band.

geophone time series, Figure 5-5, shows that most of the information carried in the signal resides in that 2-90 Hz band.

Figure 5-6 shows the measured dispersion contours and Figure 5-7 the dispersion contours determined from a best fit synthetic time series, both calculated for the best fit shot location determined by treating the PRUDEX ice cover as a single homogeneous plate. Both figures also include the exact dispersion curve calculated for the homogeneous plate's best fit inversion parameters. Two figures which demonstrate the power of SAFARI pulse modeling are the plots of synthetic and observed geophone time series for shot number 3 of series F, Figure 5-8 for the horizontal geophone and Figure 5-9 for the vertical geophone. Note in both figures that not only is the flexural wave modelled well, but also the longitudinal wave and the response to the waterborne acoustic pulse. Other arrivals seen after the longitudinal wave, but before the flexural wave are probably due to the inhomogeneity/anisotropy of the real ice and are not reflected in SAFARI modeling. Also of interest, the apparent irregular behavior on the tail of the synthetic flexural wave is introduced when the air is modeled with a realistic sound speed and density rather than treated as a vacuum; however, no set of air parameters modeled the real response well, and the air is treated as a vacuum for the remainder of this chapter.

5.3.2 Inversion of Two Abutting Infinite Half-Plates

As discussed in the previous chapter, The PRUDEX ice plate is much more accurately described as two half-plates of different thicknesses. Although a version of SAFARI able to handle some range-dependence, including inclusions in an ice plate of a different thickness than the rest of the plate, is under development during the summer of 1990 by Gerstoft and Schmidt [40], it is not available as of this writing. In order

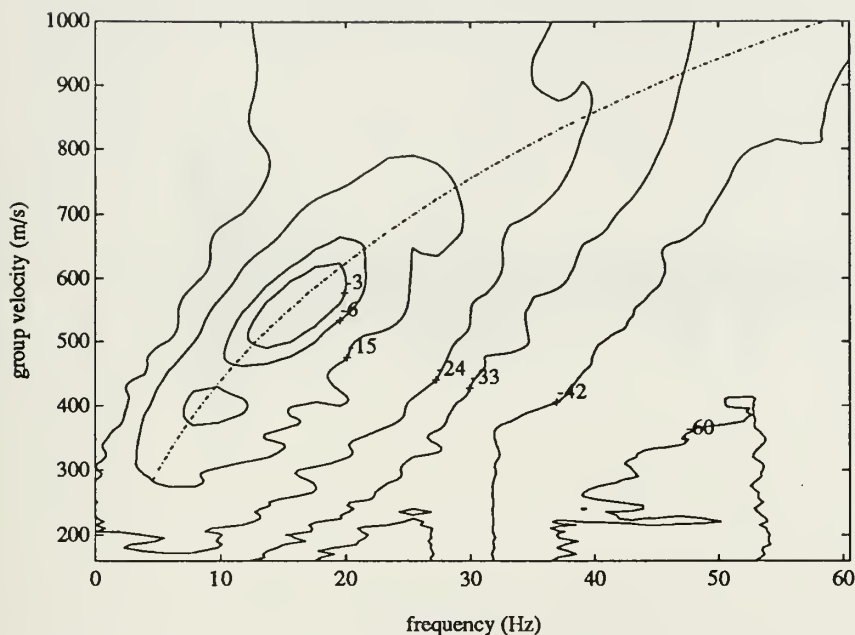


Figure 5-6: Observed contours of spectrum level (in dB normalized to 0 dB maximum) obtained by combining data from 8 shots at the PRUDEX ice camp, with the dispersion curve (-·-) calculated for $\beta=1700\text{m/s}$ and $2h=1.31$.

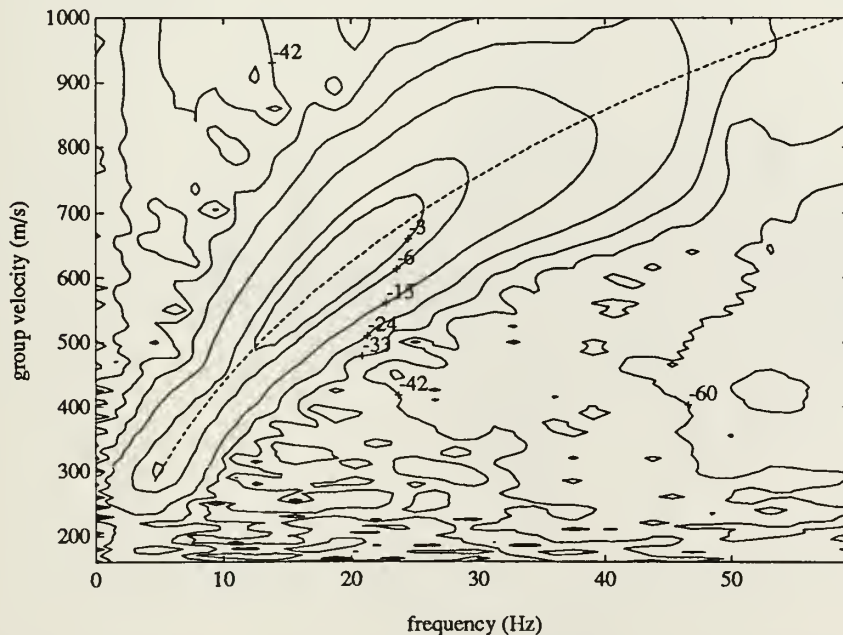


Figure 5-7: Synthetic contours of spectrum level (in dB, normalized to 0 dB maximum) derived from SAFARI time series calculated for $\alpha=3400\text{ m/s}$, $\beta=1700\text{ m/s}$, $2h=1.31\text{m}$, with corresponding exact dispersion curve (--).

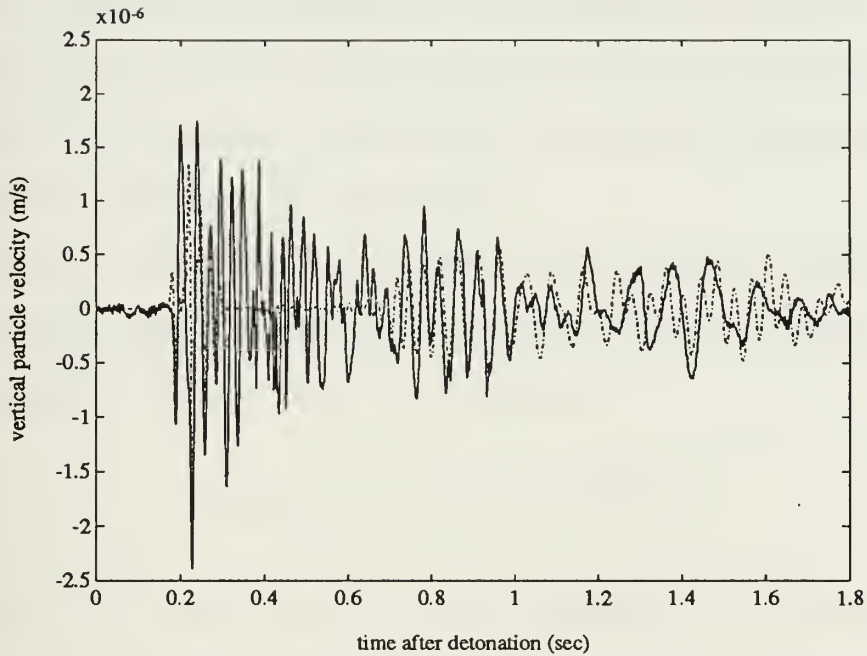


Figure 5-8: Observed response(-) on radial geophone #3 for PRUDEX shot F3; SAFARI synthetic radial response(-·-) for $\alpha=3400\text{m/s}$, $\beta=1700\text{m/s}$, $2h=1.31\text{m}$, $\gamma_\alpha=1.0\text{dB}/\lambda$, $\gamma_\beta=2.99\text{dB}/\lambda$.

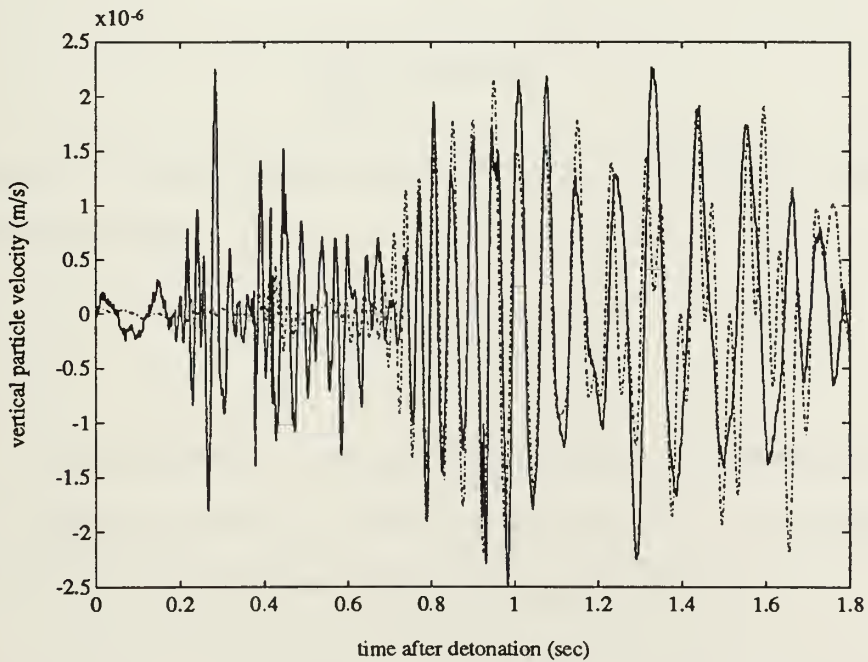


Figure 5-9: Observed response(-) on vertical geophone #3 for PRUDEX shot F3; SAFARI synthetic vertical response(-·-) for $\alpha=3400\text{m/s}$, $\beta=1700\text{m/s}$, $2h=1.31\text{m}$, $\gamma_\alpha=1\text{dB}/\lambda$, $\gamma_\beta=2.99\text{dB}/\lambda$.

to provide a rough inversion simulating the environment at the PRUDEX ice camp, a modification of the stationary phase method [4] is used in conjunction with range independent SAFARI solutions to approximate the wave form received in the second half-plate after detonation in the first half-plate.

As seen in Chapter 2, the flexural wave in an ice plate is a strongly dispersive wave of a single mode. Following the development in Aki and Richards [4], a wave packet composed of a single mode may be expressed as

$$f(x,t) = \frac{1}{2\pi} \int_{-\infty}^{\infty} |F(\omega)| e^{[-i\omega t + ik_x x + i\phi(\omega)]} d\omega, \quad (5.3)$$

where $|F(\omega)|$ is the spectral density and $\phi(\omega)$ the initial phase. In stationary phase analysis, the integration path is along the real ω axis, and for large values of x and t the integrand $\omega t + k_x x$ oscillates rapidly, with each oscillation tending to cancel the next in the integral. Only at or near a saddle point, given by

$$\frac{d}{d\omega}(-\omega t + k_x x) = 0 \quad (5.4)$$

will the phase vary slowly enough to provide a significant contribution to the integral. (5.4) can be simplified to

$$\frac{x}{t} = \frac{d\omega}{dk_x} = u, \quad (5.5)$$

where u is the group velocity. Solving (5.5) yields $\omega_s(x,t)$, the frequency expected to dominate at distance x and time t . Expanding the phase $-\omega t + k_x x$ in a Taylor series about the point $\omega = \omega_s$, and neglecting higher order terms, yields

$$-\omega t + k_x x \approx -\omega_s t + k_x(\omega_s) + \frac{x}{2} \frac{d^2 k_x}{d\omega^2} (\omega - \omega_s)^2. \quad (5.6)$$

Substituting (5.6) into (5.3), and simplifying, results in

$$f(x,t) = \frac{|F(\omega_s)|}{2\pi} \left(\frac{2\pi}{x \left| \frac{d^2 k_x}{d\omega^2} \right|} \right)^{\frac{1}{2}} e^{-i\left(\omega_s t - k_x(\omega_s)x \pm \frac{\pi}{4}\right)}, \quad (5.7)$$

where \pm corresponds to $d^2 k_x/d\omega^2 < 0$ or > 0 , respectively.

In order to apply this method to the problem of propagation in two half-plates, the stationary phase approach must be expanded to account for two propagating media. If the integrand in (5.3) is modified to reflect propagation for distances x_1 and x_2 in media with horizontal wave numbers k_{x1} and k_{x2} , then (5.4) becomes

$$\frac{d}{d\omega}(-\omega t + k_{x1}x_1 + k_{x2}x_2) = 0 \quad (5.8)$$

or

$$\frac{d}{d\omega}(-\omega t_1 + k_{x1}x_1) + \frac{d}{d\omega}(-\omega t_2 + k_{x2}x_2) = 0 \quad (5.9)$$

$$t_1 + t_2 = t$$

for which a solution is

$$\frac{x_1}{t_1} = \frac{dk_{x1}}{d\omega} \quad \wedge \quad \frac{x_2}{t_2} = \frac{dk_{x2}}{d\omega}. \quad (5.10)$$

Expanding the two relations in (5.9) in a Taylor series and adding the results yields

$$\begin{aligned} & -\omega(t_1 + t_2) + k_{x1}x_1 + k_{x2}x_2 \approx \\ & -\omega_s(t_1 + t_2) + k_{x1}(\omega_s)x_1 + k_{x2}(\omega_s)x_2 + \left[\frac{x_1}{2} \frac{d^2 k_{x1}}{d\omega^2} + \frac{x_2}{2} \frac{d^2 k_{x2}}{d\omega^2} \right] (\omega - \omega_s)^2. \end{aligned} \quad (5.11)$$

Substitution in (5.3) gives

$$f(x,t) = \frac{|F(\omega_s)|}{2\pi} \left(\frac{2\pi}{x_1 \left| \frac{d^2 k_{x1}}{d\omega^2} \right| + x_2 \left| \frac{d^2 k_{x2}}{d\omega^2} \right|} \right)^{\frac{1}{2}} e^{-i \left(\omega_s t - k_{x1}(\omega_s) x_1 - k_{x2}(\omega_s) x_2 \pm \frac{\pi}{4} \right)} \quad (5.12)$$

(5.12) does not involve attenuation, so to provide an ability to compare synthetic curves with experimental ones more directly, an additional attenuation factor is used:

$$f_a = e^{-(\delta_a k_a x + \delta_\beta k_\beta x + Ax + B)} \quad , \quad (5.13)$$

where $\delta_{\alpha,\beta} = \gamma_{\alpha,\beta} \cdot (\log e / 40\pi)$, x is the distance between the point at which the pulse spectral density is determined and the point for which the pulse is being calculated, and A and B are constants determined empirically by comparison with known results.

To demonstrate the potential accuracy of the stationary phase approach applied to the flexural wave in ice, SAFARI is used to generate synthetic time series and phase and group velocity curves for the response to an explosive shot for a given set of elastic parameters in a single homogeneous infinite floating ice plate at a ranges of 242 m and 569.5 m. The spectral density of the short range shot and the phase and group velocity curves are supplied to a computer routine which uses the stationary phase approximation (5.7) to generate the curve at the longer range. Figure 5-10 shows the short range time series, and Figure 5-11 shows the longer range time series as generated by SAFARI and as calculated from the shorter range pulse using stationary phase and the empirical amplitude attenuation of (5.13). Although the stationary phase result is not perfect, it is nonetheless good enough to allow at least an estimation of best fit curves.

To apply modified stationary phase to the problem of two abutting half-plates, a computer routine is employed which takes the SAFARI-generated phase and group

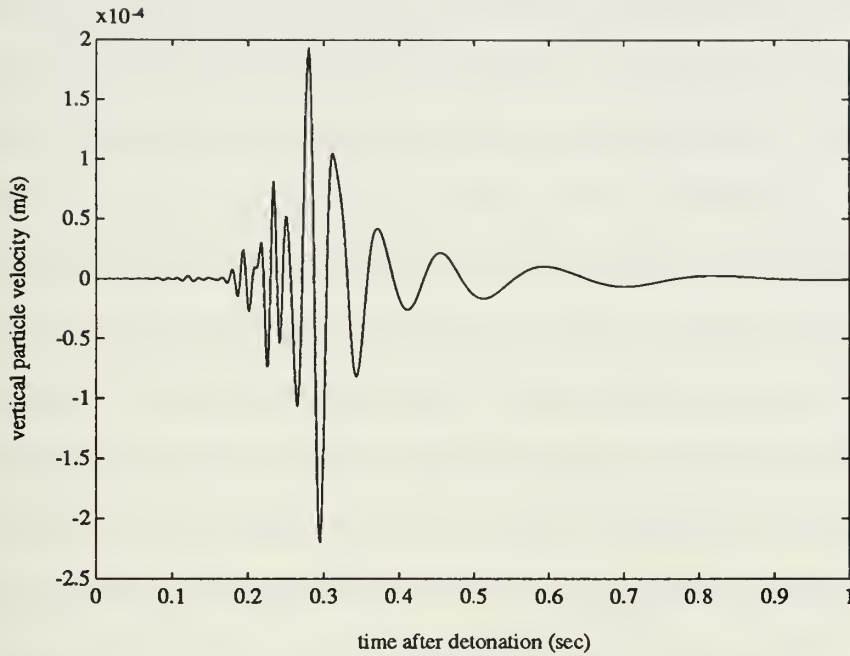


Figure 5-10: Synthetic time series for the flexural wave in a floating ice plate, calculated by SAFARI for $\alpha=3500\text{m/s}$, $\beta=1750\text{m/s}$, $2h=2.4\text{m}$, $\gamma_\alpha=1.0\text{dB}/\lambda$, $\gamma_\beta=2.99\text{dB}/\lambda$ at a range of 242m.

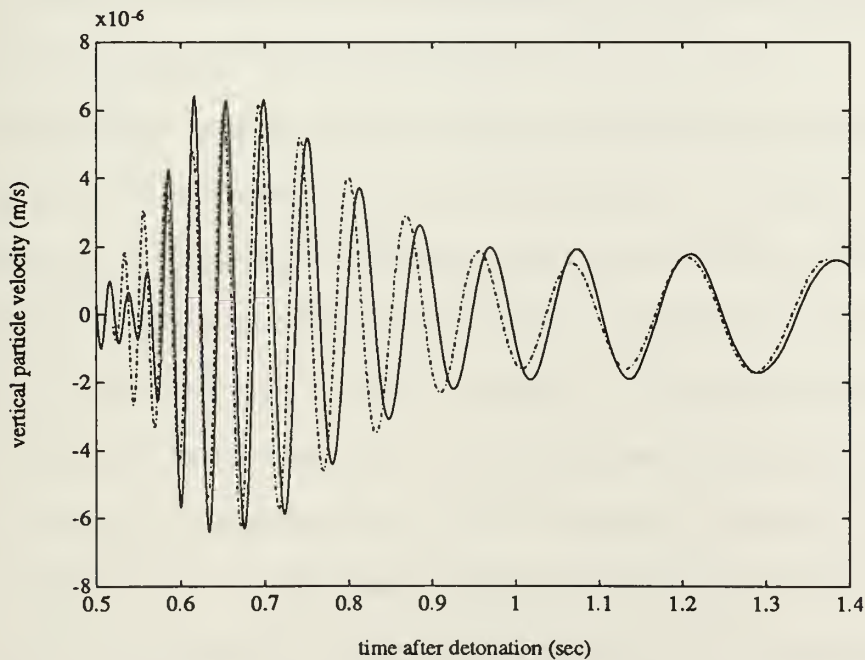


Figure 5-11: SAFARI synthetic time series(-) for parameters of Figure 5-10 at a range of 569.5m, and time series(-·-) generated by applying the method of stationary phase to Figure 5-10.

velocities for the flexural wave in the two half-plates along with the orientation of the ridge line separating the two halves and determines as a function of frequency the index of refraction and the path from the shot location to a given geophone. The routine uses the calculated path, the supplied spectral density of the shot determined from a time series generated for the travel distance in the first plate, and the phase and group velocity curves to construct using (5.12) the time series as received at the geophone in the second plate. This synthetic time series for the flexural wave can now be compared with the observed time series to adjust model parameters and proceed with the inversion.

Reliance on the flexural wave for inversion resurrects the problem of shear velocity/ice thickness ambiguity discussed earlier. To establish a reasonable anchor on shear velocity, the location routine is used to investigate the best fit SH wave speed in the two plates. Assuming that the SH wave is excited directly by the shot and there is no anisotropy, this value can be used directly as the shear velocity in the respective plates. The best fit consistent with the longitudinal wave's index of refraction of 1.12 is $\beta_1=1590$ m/s, and $\beta_2=1750$ m/s, for an index of refraction of 1.10.

The modified stationary phase procedure introduced above adds an additional ambiguity to the inversion problem at any given geophone. A best fit curve can be generated by any one of a family of solutions whose flexural wave velocity curves and resulting index of refraction combine to produce the same radial velocity from source to receiver. If the second plate is truly a homogeneous half-plate of constant thickness, then this ambiguity can be resolved with the straightforward but laborious procedure of locating the best fit simultaneously at all four geophone locations; unfortunately, apparent variations in the second plate's thickness have prevented finding any set of parameters for the second plate which provide a good fit at all, or even most geophones. This problem is not surprising in light of the significant variation in ice thickness

calculated at each geophone in Chapter 4, and displayed in Table 4-1. To determine the correct solution, the location routine is used to determine the best index of refraction for the flexural wave, given the shot location and the orientation of the ridge line. The best fit solutions with indexes of refraction centered about this value are chosen, assuming a constant thickness in the first plate, but an average thickness varying with geophone path in the second.

Figure 5-12 through Figure 5-15 show the best fit flexural wave time series at each of the four vertical geophones, along with the experimentally observed time series. Since no geophone calibration data is available, a best fit geophone calibration factor of 10^{-5} m/s/volt is applied to all four geophone outputs to allow comparison of calculated and observed time series. Solutions at the four geophones are summarized in Table 5-2. Figure 4-5 shows that the ray path from the shot location to geophone #1

	Geophone Nr			
Parameter	1	2	3	4
α_1 (m/s)	3000			
β_1 (m/s)	1590			
$\gamma_\alpha, \gamma_\beta$ (db/ λ)	1.0, 2.66			
$2h_1$ (m)	1.18			
α_2 (m/s)	3500			
β_2 (m/s)	1750			
$\gamma_\alpha, \gamma_\beta$ (db/ λ)	1.0, 2.99			
$2h_2$ (m)	2.40	2.37	2.15	2.20

Table 5-2: Best compressional/shear velocities and attenuations and plate thicknesses determined by treating the PRUDEX ice cover as two abutting half-plates, with the shot conducted under plate 1, and the receiving array on plate 2.

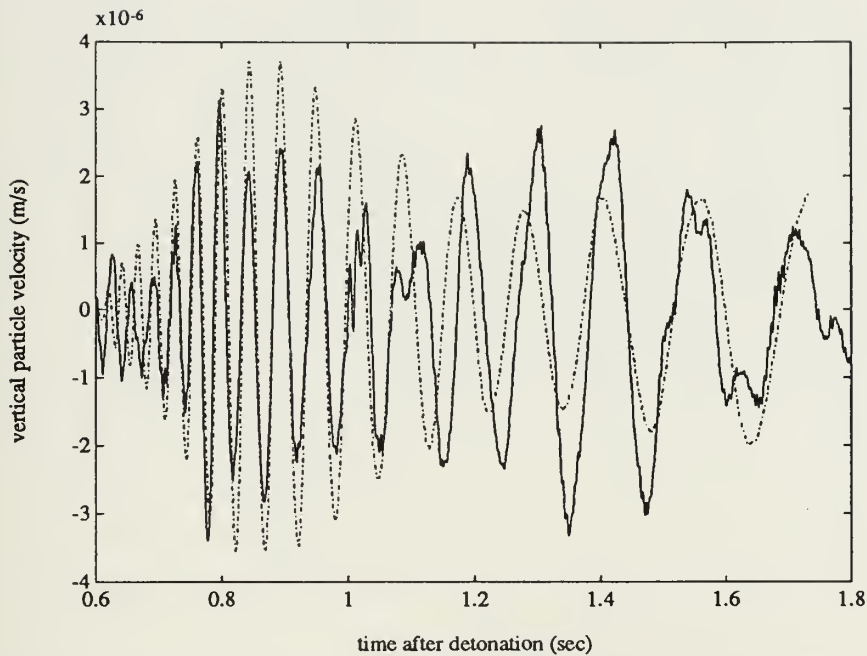


Figure 5-12: Observed flexural wave time series(-) for PRUDEX shot F3 at vertical geophone #4, and synthetic time series(-·-) for shot F3 at geophone #4 developed using the parameters of Table 5-2.

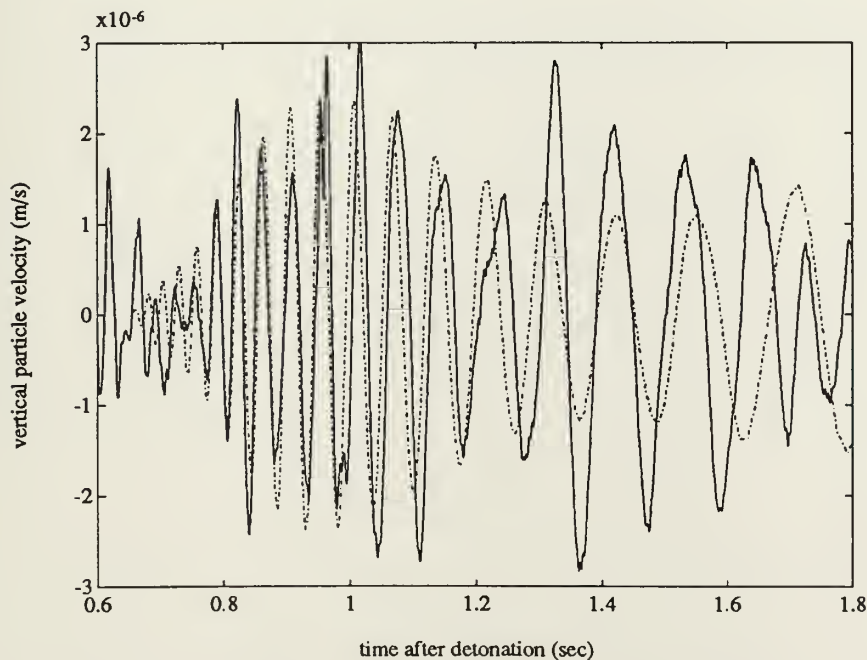


Figure 5-13: Observed flexural wave time series(-) for PRUDEX shot F3 at vertical geophone #3, and synthetic time series(-·-) for shot F3 at geophone #3 developed using the parameters of Table 5-2.

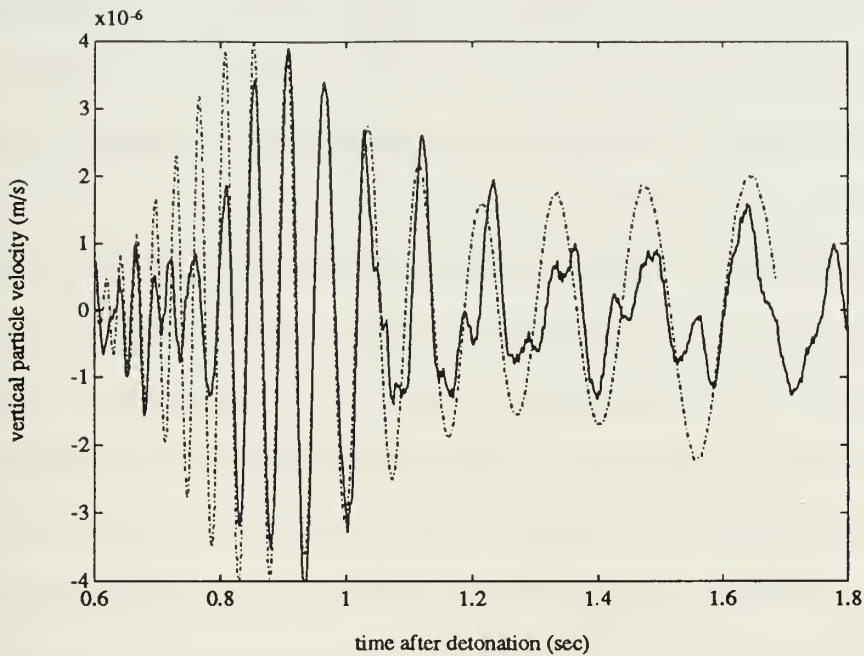


Figure 5-14: Observed flexural wave time series(-) for PRUDEX shot F3 at vertical geophone #1, and synthetic time series(-·-) for shot F3 at geophone #1 developed using the parameters of Table 5-2.

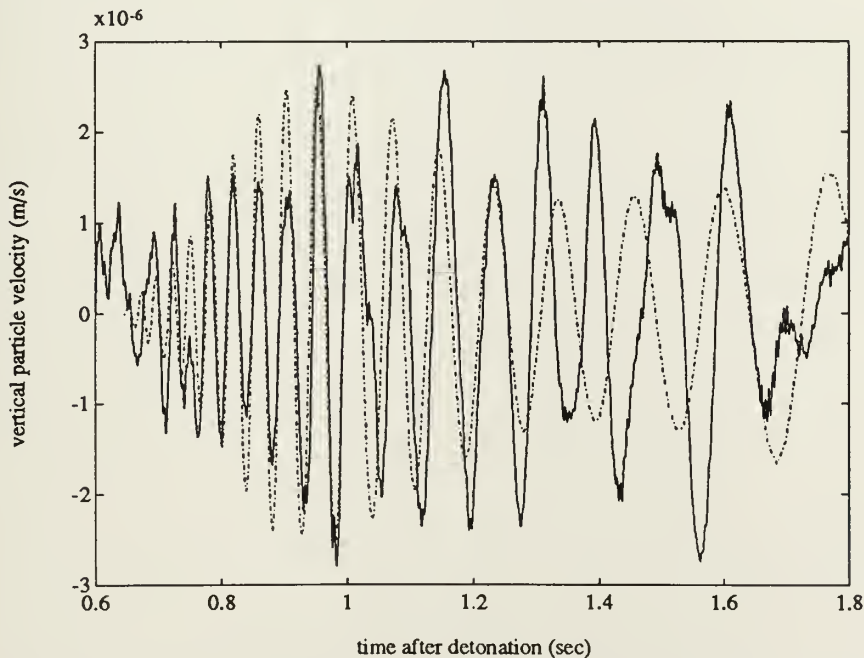


Figure 5-15: Observed flexural wave time series(-) for PRUDEX shot F3 at vertical geophone #2, and synthetic time series(-·-) for shot F3 at geophone #2 developed using the parameters of Table 5-2.

nearly coincides with the path to geophone #2, and that the path to geophone #3 follows exactly the path to geophone #4. Given that Table 5-2 shows that the average ice thickness seen by geophones #2 and #3 is less than that seen by geophones #1 and #4, the observation that the best fit thickness at geophones #2 and #3 is less than that for geophones #1 and #4 is a confirmation of at least the general validity of these results. Even so, uncertainties inherent in the determination of the shot location and the orientation of the ridge line, as well as in the application of the modified stationary phase procedure and the inversion process itself, all combine to render the values of Table 5-2 as no more than estimates of elastic parameters at the PRUDEX ice camp. While Table 5-2 should provide a fair representation of that environment, due to the complex interaction of factors involved in their derivation, it is not possible to assign definite uncertainties to these parameters.

Chapter 6

Conclusion

The final chapter summarizes the significant results of Chapters 3, 4 and 5, and makes some recommendations for future work.

6.1 Summary

Work with the propagation data generated at the PRUDEX ice camp has yielded a number of significant findings which contribute directly to the body of knowledge of seismo-acoustic propagation in the Arctic Ocean. This work has also highlighted the importance of certain tools in the furtherance of that knowledge.

6.1.1 Elastic Parameters of the Arctic Ice

The values of bulk compressional and shear wave speeds obtained for the thicker multi-year ice at the PRUDEX ice camp, 3500 m/s and 1750 m/s, respectively, compare very well with similar values obtained by earlier investigators. It is also interesting to note that the shear speed measured in the annual ice, 1590 m/s, is considerably lower than in the thicker ice, although not as low as some investigators have predicted [41].

The work with the PRUDEX data vigorously supports the assertion that useful values for the low frequency elastic parameters of arctic sea ice cannot be obtained from laboratory measurements or extrapolations from related data. Attenuation values of about 1 dB/ λ for the compressional wave, and 3 dB/ λ for the shear wave, as estimated

in this work, are slightly higher than but consistent with values reported by the two previous *in situ* studies [31][14]; however, these values are more than four time greater than the best available numbers estimated using laboratory and other data [22].

6.1.2 Propagation Mechanisms

Study of the PRUDEX data has revealed the presence of strong horizontally polarized transverse (SH) waves propagating in the sea ice canopy as a result of small underwater explosive detonations. Since the theory of plate wave propagation has no mechanism for coupling SH waves in a plate with acoustic waves in an adjacent liquid, these waves are entirely unexpected and as yet unexplained. The PRUDEX data sets generally support the contention that these waves originate in the ice canopy at or very near the time and horizontal location of the detonation. The data sets do not support SH wave generation by out-of-plane scattering during the interaction of either longitudinal, flexural or waterborne waves with the ridge line identified in the ice sheet.

This study also has included the first identification of the horizontal refraction of a family of wave types propagating in a sheet of arctic ice. Each of the wave types appears to obey simple Snell's law refraction at the linear abutment between the two half-plates which comprise the ice canopy, refracting at angles appropriate to the different wave speeds in the two half-plates.

6.1.3 Analysis Tools

One of the most useful lessons highlighted during analysis of the PRUDEX data was the striking superiority of a simple system of four 3-axis geophones over a system of nine hydrophones in a larger array. Not only was the geophone array dramatically superior in localizing the underwater detonations which excited elastic waves in the ice,

it also allowed the detection and study of wave types and propagation phenomenon not visible in the hydrophone data. The ability of the geophone array to isolate several different wave types traveling at different speeds placed a much stronger bound on possible ranges and bearings from the array center to the shot location than did the hydrophone array's reception of the single waterborne wave, despite the fact that the hydrophone array was larger and the pulse arrivals could be measured more accurately by the processing system. The detection of the SH waves by the geophone array, as well as the strong and clear reception of both longitudinal waves and flexural waves, could not have been accomplished from hydrophone data. Indeed, tomographic studies of acoustic propagation under the arctic ice have shown that the characteristics of the ice cover appear primarily as second order effects (*e.g.*, beam displacement of the reflected waterborne pulse) in the hydrophone data [42][43]. Clearly, a geophone array is a superior tool for use in studies of seismo-acoustic propagation in a localized section of sea ice.

Inversion of the PRUDEX data has also served to reemphasize the value of SAFARI numeric modeling in seismo-acoustic propagation problems. In a homogeneous plate the results of Chapter 5 indicate that SAFARI is capable of fully and accurately reproducing all of the elements of the real seismo-acoustic signature: the longitudinal wave, the flexural wave, and even the response to the waterborne acoustic wave as it passes beneath the geophones.

Finally, a potentially useful tool to extend two-dimensional SAFARI to a range-dependent environment, the modified stationary phase approximation of the flexural wave (or any highly dispersive wave), has been demonstrated. This method serves as an effective if somewhat limited interim fix for the solution to propagation in two adjacent plates until such time as development of the next generation of SAFARI-like

algorithms is complete.

6.2 Future Work

The great variation in the sea ice elastic parameters determined in the vicinity of the PRUDEX ice camp, as well as the general and temporal variability reported recently by Brooke and Ozard [31] and earlier by Hunkins [24], all indicate that more work in this area is appropriate in order to establish a set of parameters which characterize the arctic environment accurately over a given area and season. This thesis has shown that in a well-surveyed homogeneous environment (*i.e.*, with all geometric uncertainties eliminated), basic SAFARI modeling of under-ice detonations is readily capable of yielding very accurate determinations of bulk shear and compressional velocities and attenuations from geophone data obtained *in situ*.

If obtaining geophone measurements in sufficient number and at enough locations to accurately characterize the arctic environment proves to be impractical, other approaches, such as ocean acoustic tomography, may also be capable of obtaining average values of the elastic parameters over large areas. High frequency cross-hole tomography conducted directly in the ice [29] can shed additional light on the variability of the anelastic properties of sea ice, although extending such results to the low frequencies of interest in this work will remain a problem. These approaches certainly warrant further investigation.

Much more work remains to be done to determine the mechanism which couples acoustic waves in the water with SH waves in the plate. An important element in this work should be under-ice explosive shots made with geophone detectors installed not only at a central array, but spread in range along the propagation path. Additionally, under-ice surveys should be conducted to identify discontinuities in the ice canopy not

visible on its upper surface. The information available in this expanded experiment may well prove vital to isolating the interaction which generates the SH waves.

In order to further study seismo-acoustic propagation in arctic ice in a range-dependent environment, it will be necessary to bring advanced versions of SAFARI, now in development [40], to bear on the problem. In this way experimental measurements will not necessarily be limited to strictly homogeneous environments, and data sets taken in complex environments, such as that of the PRUDEX ice camp, can be inverted with more confidence and reliability than is possible with the limited tools now available.

References

- [1] F. DiNapoli and R.H. Mellen. Low Frequency Attenuation in the Arctic Ocean. Ocean Seismo-Acoustics. Edited by T. Akal and J. Berkson. Plenum Press, New York, 1986.
- [2] H. Schmidt and F.B. Jensen. A Full Wave Solution for Propagation in Multilayered Viscoelastic Media with Application to Gaussian Beam Reflection at Fluid-Solid Interfaces. *Journal of the Acoustical Society of America* 77: 813-825, 1985.
- [3] H. Schmidt. *SAFARI Seismo-Acoustic Fast field Algorithm for Range-Independent environments User's Guide*. SACLANTCEN Report SR-113. SACLANT Undersea Research Center, San Bartolomeo, Italy, 1988.
- [4] K. Aki and P.G. Richards. *Quantitative Seismology*. W.H. Freeman and Company, New York, 1980.
- [5] M. Ewing, A.P. Crary and A.M. Thorne, Jr. Propagation of Elastic Waves in Ice. Part I. *Physics* 5: 165-168, 1934.
- [6] M. Ewing and A.P. Crary. Propagation of Elastic Waves in Ice. Part II. *Physics* 5: 181-184, 1934.
- [7] K.F. Graff. *Wave Motion in Elastic Solids*. Ohio State University Press, 1975.
- [8] G.B. Thomas, Jr. *Calculus and Analytic Geometry*, 4th Edition. Addison-Wesley Publishing Co., Reading, MA, 1968.
- [9] R.D. Mindlin. Waves and Vibrations in Isotropic Elastic Plates. *Structural Mechanics, Proceedings of the First Symposium on Naval Structural Mechanics*. Edited by J.N. Goodier and N.J. Hoff. Pergamon Press, New York, 1960.
- [10] W.M. Ewing, W.S. Jardetzky and F. Press. *Elastic Waves in Layered Media*. McGraw-Hill Book Company, Inc., New York, 1957.
- [11] M. Redwood. *Mechanical Waveguides*. Pergamon Press, New York, 1960.
- [12] F. Press and M. Ewing. Propagation of Elastic Waves in a Floating Ice Sheet. *Transactions, American Geophysical Union* 32: 673-678, 1951.

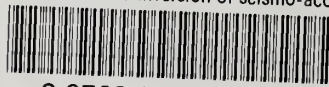
- [13] A.J. Langley. Exact and Approximate Theories for Fluid-Loaded, Infinite, Elastic Plates. *Journal of the Acoustical Society of America* **83**: 1366-1376, 1988.
- [14] P.J. Stein. Acoustic Monopole in a Floating Ice Plate. PhD thesis, Massachusetts Institute of Technology and the Woods Hole Oceanographic Institution, February, 1986.
- [15] C.L. Pekeris. Theory of Propagation of Explosive Sound in Shallow Water. *Memoirs, Geological Society of America* **27**, 1948.
- [16] M.G. McPhee. PRUDEX Turbulence Cluster/Acoustic Current Meter Comparison, Including Drift, Wind, and CTD Data, A report prepared for Polar Science Laboratory, University of Washington. McPhee Research Company, Yakima, WA, 31 July 1987.
- [17] K. von der Heydt. *Optical Disk based Acquisition System (ODAS)*. Technical Report WHOI-87-49, Woods Hole Oceanographic Institution, 1987.
- [18] K.E. Prada, K. von der Heydt and T.F. O'Brien. A Versatile Multi-Channel Data Acquisition System for Seismic and Acoustic Applications. *In Proceedings of the IEEE Conference Oceans '81*: 44-47, 1981.
- [19] R.J. Urick. *Principles of Underwater Sound*, 3d Edition. McGraw-Hill Book Company, New York, 1983.
- [20] E.K. Scheer, A.B. Baggeroer and H. Schmidt. Preliminary CEAREX data analysis notes. Woods Hole Oceanographic Institution, Woods Hole, MA, Spring 1990.
- [21] W.H. Press, B.P. Flannery, S.A. Teukolsky and W.T. Vetterling. *Numerical Recipes*. Cambridge University Press, 1986.
- [22] D.F. McCammon and S.T. McDaniel. The Influence of the Physical Properties of Ice on Reflectivity. *Journal of the Acoustical Society of America* **77**: 499-507, 1985.
- [23] F. Press, A.P. Crary, J. Oliver and S. Katz. Air-Coupled Flexural Waves in Floating Ice. *Transactions, American Geophysical Union* **32**: 166-172, 1951.
- [24] K. Hunkins. Seismic Studies of Sea Ice. *Journal of Geophysical Research* **65**: 3459-3472, 1960.
- [25] A.P. Crary. Seismic Studies on Fletcher's Ice Island, T-3. *Transactions, American Geophysical Union* **35**: 293-300, 1954.

- [26] J.A. Westphal. In Situ Acoustic Attenuation Measurements in Glacial Ice. *Journal of Geophysical Research* **70**: 1849-1853, 1965.
- [27] T.K. Clee, J.C. Savage and K.G. Neave. Internal Friction in Ice near its Melting Point. *Journal of Geophysical Research* **74**: 973-980, 1969.
- [28] M. P. Langleben. Attenuation of Sound in Sea Ice, 10-500 kHz. *Journal of Glaciology* **8**: 399-406, 1969.
- [29] S.D. Rajan, J.A. Doust and G.V. Frisk. Determination of Compressional and Shear Wave Speed Profiles in Sea Ice. *Journal of the Acoustical Society of America* **87**(S1): S84, 1990. (Abstract only).
- [30] P.J. Stein. Interpretation of a Few Ice Event Transients. *Journal of the Acoustical Society of America* **83**: 617-622, 1988.
- [31] G.H. Brooke and J.M. Ozard. In-situ Measurement of Elastic Properties of Sea Ice. *Underwater Acoustic Data Processing*. Edited by Y.T. Chan. Kluwer Academic Publishers, 1989.
- [32] J. Schwarz and W.F. Weeks. Engineering Properties of Sea Ice. *Journal of Glaciology* **19**: 499-531, 1977.
- [33] F.B. Jensen and H. Schmidt. Shear Properties of Ocean Sediments Determined from Numerical Modelling of Scholte Wave Data. *Ocean Seismo-Acoustics*, Edited by T. Akal and J.M. Berkson. Plenum Press, New York, 1985.
- [34] M.B. Priestly. *Spectral Analysis and Time Series*. Academic Press, London, 1981.
- [35] J. Wakeley, Jr. Pressure-Signature Model for an Underwater Explosive Charge. *Journal of Underwater Acoustics* **27**: 445-449, 1977.
- [36] Commander, Naval Sea Systems Command. *Demolition Materials*, NAVSEA Publication SW060-AA-MMA-010, Change A. Naval Sea Systems Command, 1985.
- [37] R.H. Cole. *Underwater Explosions*. Princeton University Press, 1948.
- [38] A.V. Oppenheim and R.W. Shafer. *Discrete-Time Signal Processing*. Prentice Hall, Englewood Cliffs, NJ, 1989.
- [39] L.R. Rabiner and B. Gold. *Theory and Application of Digital Signal Processing*. Prentice Hall, Englewood Cliffs, NJ, 1975.

- [40] P. Gerstoft and H. Schmidt. A Boundary Element Approach to Ocean Seismo-Acoustic Facet Reverberation. Submitted to the *Journal of the Acoustical Society of America*.
- [41] W.A. Kuperman and H. Schmidt. Rough Surface Elastic Wave Scattering in a Horizontally Stratified Ocean. *Journal of the Acoustical Society of America* **79**: 1767-1777, 1986.
- [42] Jin Guoliang and P. Wadhams. Travel Time Changes in a Tomographic Array Caused by a Sea Ice Cover. *Progress in Oceanography* **22**: 249-275, 1989.
- [43] B.E. Miller. Travel Time Changes in Arctic Tomography by Full Wavefield SAFARI Solution. Project Report for Subject 13.851, Ocean and Seabed Acoustics II, Massachusetts Institute of Technology, May, 1990.

thesM58566

Observation and inversion of seismo-acou



3 2768 000 89280 6

DUDLEY KNOX LIBRARY